University of Tennessee, Knoxville
Trace: Tennessee Research and Creative Exchange

Doctoral Dissertations | Graduate School

12-2006

Pseudoelasticity and Shape Memory Effect in Single Crystal Fe_3Al

Saurabh Kabra
University of Tennessee - Knoxville

Recommended Citation

Kabra, Saurabh, "Pseudoelasticity and Shape Memory Effect in Single Crystal Fe_3Al. " PhD diss., University of Tennessee, 2006.
https://trace.tennessee.edu/utk_graddiss/1989

This Dissertation is brought to you for free and open access by the Graduate School at Trace: Tennessee Research and Creative Exchange. It has been accepted for inclusion in Doctoral Dissertations by an authorized administrator of Trace: Tennessee Research and Creative Exchange. For more information, please contact trace@utk.edu.

To the Graduate Council:

I am submitting herewith a dissertation written by Saurabh Kabra entitled "Pseudoelasticity and Shape Memory Effect in Single Crystal Fe_3Al." I have examined the final electronic copy of this dissertation for form and content and recommend that it be accepted in partial fulfillment of the requirements for the degree of Doctor of Philosophy, with a major in Materials Science and Engineering.

Easo P. George, Major Professor

We have read this dissertation and recommend its acceptance:

Dayakar Penumadu, George M. Pharr, Peter K. Liaw

Accepted for the Council:
Carolyn R. Hodges

Vice Provost and Dean of the Graduate School

(Original signatures are on file with official student records.)

To the Graduate Council:

I am submitting herewith a dissertation written by Saurabh Kabra entitled "Pseudoelasticity and Shape Memory Effect in Single Crystal Fe_3Al". I have examined the final electronic copy of this dissertation for form and content and recommend that it be accepted in partial fulfillment of the requirements for the degree of Doctor of Philosophy, with a major in Materials Science and Engineering.

Easo P. George

Major Professor

We have read this dissertation and
recommend its acceptance:

Dayakar Penumadu

George M. Pharr

Peter K. Liaw

Accepted for the Council:

Linda Painter

Interim Dean of Graduate Studies

(Original signatures are on file with official student records)

Pseudoelasticity and Shape Memory Effect in Single Crystal Fe_3Al

A Dissertation

Presented for the

Doctor of Philosophy Degree

The University of Tennessee, Knoxville

Saurabh Kabra

December 2006

To my parents whose love has kept me going and to

chacha who inspired the scientist in me

Acknowledgements

Firstly, I wish to thank Dr. Easo P. George for giving me this wonderful opportunity as a PhD student at the University of Tennessee and Oak Ridge National Laboratory. Not only did he inspire me as a scientist but also as a philosopher. I also thank him for the guidance and freedom he gave throughout this project.

I need to give special thanks to Dr. Hongbin Bei and Dr. Donald W. Brown who have been heavily involved with the current work. Hongbin has been involved in a number of experiments reported in this dissertation. Don has helped with neutron diffraction related experiments and analysis and given some valuable inputs.

A number of people have helped in technical and non-technical ways throughout my PhD years. These include many group members, graduate students, technical staff, administrative staff and others. The most important among these are Dr. Aravind Gali, Mr. Cecil Carmichael, Dr. Elliot Specht, Mr. Elmer Lee, Mr. Joe Wright, Dr. Mark A. M. Bourke, Dr. Mike West, Dr. Robert D. Field, Ms. Sherry Samples, Ms. Sujing Xie, Dr. Sven Vogel, Mr. Thomas Sisneros and Dr. Yukinori Yamamoto.

I wish to thank the Basic Energy Sciences program of the US Department of Energy for providing funds for myself as well as the project.

Abstract

Fe_3Al is an intermetallic compound which has shown some excellent engineering properties and has been widely studied for this reason. It also shows interesting mechanical phenomenon like yield stress anomaly and pseudoelasticity. Mechanical behavior and diffraction studies on the pseudoelastic aspect of Fe_3Al have been presented in this work.

Single crystalline, $D0_3$ ordered Fe_3Al is known to show pseudoelastic behavior at room temperature. Pseudoelastic behavior was seen in both tension and compression with a distinct tension-compression asymmetry. No strain hardening occurred under tension even at high applied strains as opposed to compression, where the alloy strain hardened continuously. In-situ observations on the surface revealed reversible features indicating activity on the (211) planes.

The tensile stress-strain curve shows notable changes with varying temperature. At very low temperatures (~100 K) shape memory effect is seen for small amounts (~3% in compression) of applied strain. At high temperatures (~393 K) pseudoelasticity is lost and plasticity commences. Between these two extremes, the reverse stress (stress during strain recovery) follows the Clausius-Clayperon type relationship with temperature but the forward stress remains unchanged.

In-situ Neutron Diffraction experiments in both tension and compression show large reversible changes in the diffraction pattern upon loading. Intensities and position of various peaks changed reversibly by large amounts during the load-unload cycle. All changes in the diffraction pattern revert back close to the original pattern upon unloading.

These changes are closely correlated to the load-unload stress-strain curve. These large changes in the diffraction pattern point towards major structural changes inside the crystal and cannot be explained by elastic effects alone.

Closer inspection revealed the appearance of new peaks and satellite reflections on loading, which disappeared upon unloading. Diffraction experiments point towards a phase transformation which might be responsible for the pseudoelastic behavior in Fe_3Al.

Table of Contents

List of Tables

List of Figures

Chapter # 1

Mechanical Properties of Ordered Alloys: Pseudoelasticity in Fe_3Al

1.1 Ordered intermetallics

Intermetallics alloys are chemical compounds between two or more metals. Intermetallics are unique in the sense that the structure and properties displayed by them could be quite different from those of its constituents [1-3]. Therefore, even though we begin with simple metals we end up with properties which are quite different and in some respects more desirable than those of either of the constituent metals.

Intermetallics show mixed bonding comprising of metallic and ionic/covalent character and a strong internal order, which can be long range or short range in nature. The presence of order introduces many structural features like superpartial dislocations, anti phase boundaries (APB), anti domain boundaries (APD) etc. All these factors greatly affect the macroscopic physical properties, including mechanical, magnetic, and electrical.

Intermetallics have been studied extensively for structural applications. They promise a compromise between ceramic (strength) and metallic (ductility) properties. Intermetallics are specially suited for high temperature applications because they are

much better at retaining strength at high temperatures as compared to other alloys. Some intermetallics have been successfully used for high temperature structural applications (e.g. Ni_3Al [4]).

The study of intermetallics has also aided the development of novel material like shape memory alloys (SMA)[5]. Other intermetallics display good magnetic properties [6] and superconductivity [7].

While intermetallics are of immense engineering interest, they are interesting systems also from a scientific point of view. With respect to the mechanical properties it is scientifically interesting to understand how the ordering-related aspects (e.g. superpartials, APBs, APDs) of these alloys influence the deformation mechanisms and thus the macroscopic behavior. Knowledge of these mechanisms also enables engineers to design alloys with improved macroscopic properties.

In this work some specific aspects of the mechanical properties of $D0_3$-ordered Fe_3Al namely its pseudoelasticity has been studied.

1.2 Properties of ordered alloys

In alloys it is sometimes thermodynamically favorable for compounds to form at or near definite atomic ratios (e.g. AB, A_3B) below some critical temperature [2]. These are the intermetallic phases. Shown in figure 1.1 are four widely studied ordered lattices. Table 1.1 lists some common alloys in which these phases are known to occur [8].

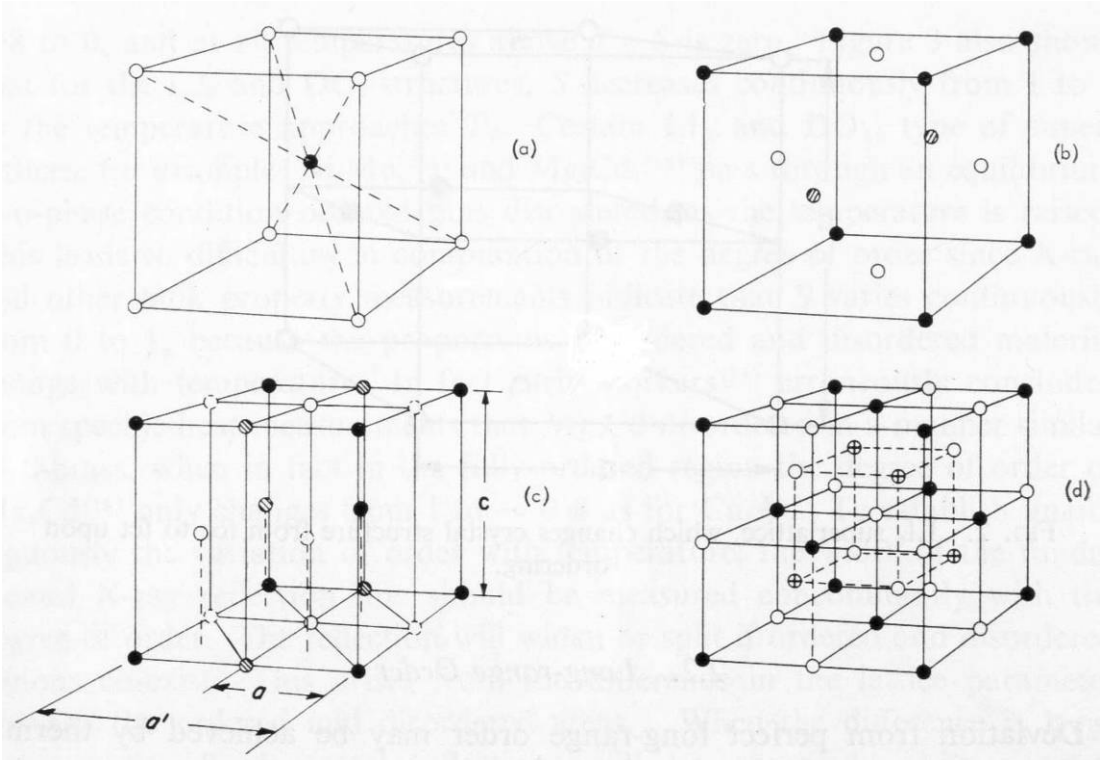

Figure 1.1 Crystal structures of (a) B2 (b) $L1_2$ (c) $D0_{19}$ (d) $D0_3$ [8] ordered alloys.

Table 1.1 Examples of some intermetallic alloys which crystallize in the crystal structure shown in Figure 1.1 [8].

Structure Type	Examples
B2	CuZn, FeCo, NiAl, CoAl, FeAl, AgMg
$L1_2$	Cu_3Au, Au_3Cu, Ni_3Mn, Ni_3Fe, Ni_3Al, Pt_3Fe
$D0_{19}$	Mg_3Cd, Cd_3Mg, Ti_3Al, Ni_3Sn
$D0_3$	Fe_3Al, Fe_3Si, Fe_3Be, Cu_3Al
$L1_0$	AuCu, CoPt, FePt, FePd

The complex lattices can be viewed as a combination of interpenetrating simpler lattices. For example the B2 lattice can be seen as two interpenetrating simple cubic lattices. Similarly, $D0_3$ can be seen as two interpenetrating FCC lattices.

1.2.1 Long range and short range order

In an ordered alloy, each type of atom can occupy to certain fixed sites in the crystal lattice throughout the alloy. This is known as long range order. For perfect long range order, each atom sits at its designated position in accordance with the crystal structure. The long range order parameter for a binary *A*-*B* alloy [9] is defined as

$$S = \frac{p - r}{1 - r} \tag{1-1}$$

where p is the probability that an A atom site is filled by an A atom and r is the fraction of the total sites that are occupied by A atoms for perfect order. This parameter can vary from 0 to 1, 0 for perfectly disordered alloy and 1 for perfectly ordered alloy.

The order parameter changes with the temperature, heat treatment and composition of the alloy. On heating, the order changes from 1 to 0 as the temperature approaches the order-disorder temperature, T_c. This can happen slowly or suddenly as shown for B2 (β brass) and $L1_2$ (Cu_3Au) structures in Figure 1.2

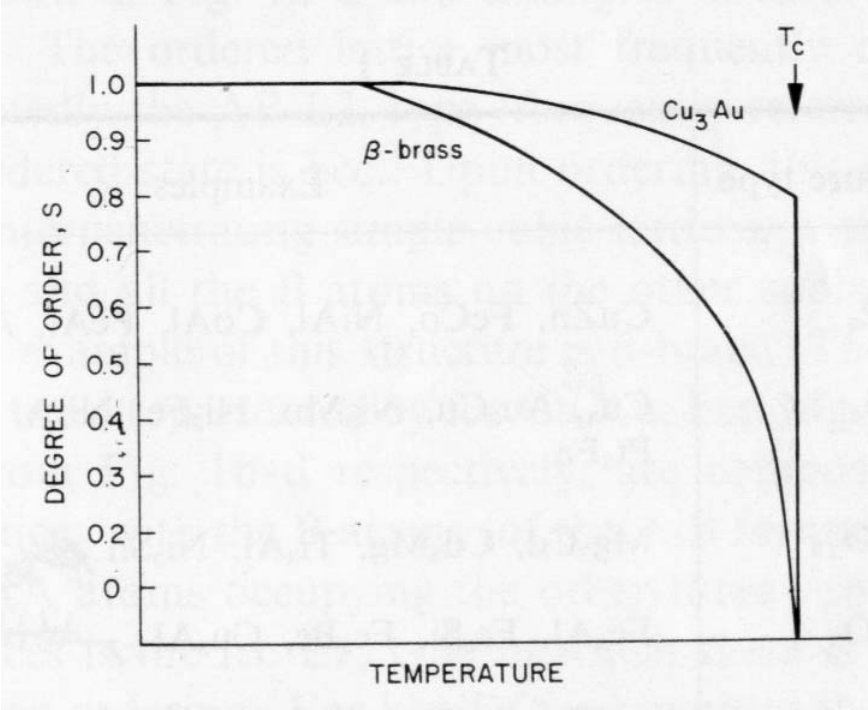

Figure 1.2 Variation of long range order with temperature in β brass (B2) and Cu_3Au ($L1_2$) [8].

Above T_c considerable amount of short range order is found. This means that the probability of finding unlike atoms sitting near each other is more than that predicted by a completely random distribution of atoms on lattice sites. In most cases specimens quenched from above T_c also retain short range order.

1.2.2 Superpartial dislocations and anti phase boundary (APB)

The structure of an ordered alloy has a lower symmetry than its disordered counterpart. The lattice of an ordered structure is known as a superlattice, where 'super' signifies only the fact that certain types of atoms occupy certain lattice sites. As a

consequence of the lower symmetry, extra reflections appear in the diffraction pattern known as “superlattice reflections”.

Partial dislocations and anti phase boundaries (APB) will be described in detail later in this chapter but needs to be brief mention is warranted at this point. When a full dislocation passes on a certain plane in either an ordered or a disordered structure, the lattice is restored after the dislocation has passed. Consider the case of a partial dislocation moving in an ordered lattice (or superlattice). Upon passage of the partial dislocation the order is disrupted in the plane on which the dislocation has passed. This means that the arrangement (in terms of order only) of atoms on either side of the partial dislocation is not the same. These dislocations are now known as superpartial dislocations.

Note that upon the passage of a partial in a disordered lattice or a single element lattice the atomic arrangement would be the same on either side of the partial dislocation. The formation of a stacking fault can occur upon the passage of partials in a disordered lattice but this will not be discussed here.

In an ordered alloy full dislocations dissociate into superpartial dislocations. The region between the superpartials where the order is disrupted as compared to the rest of the lattice is known as an anti phase boundary (APB) region. The separation of the superpartials or the width of the APB is determined by the APB energy.

1.2.3 Anti phase domains (APD)

Ordering occurs both by nucleation and growth, and homogenously, in different alloys upon lowering of the temperature. For example, in a B2 lattice, ordering is generally homogenous but a nucleation and growth type mechanism is seen in most $L1_2$ lattice. In a nucleation and growth model, highly ordered regions nucleate within the disordered matrix upon lowering of the temperature below T_c which grow until they contact each other. Homogenous ordering occurs by an increase in the number of unlike bonds throughout the matrix with decreasing temperature. For a given system, one of the above models is dominant but they do posses some characteristics of each other. For example, ordering occurs homogeneously in Fe_3Al upon continuous cooling but by nucleation and growth isothermally.

The small ordered regions which nucleate at different sites grow into ordered domains. These domains meet each other at planes where the order is disrupted. These planes are similar to APBs and are often referred to as APBs. The ordered domains are known as anti phase domains (APD) or simply domains. Figure 1.3 shows some examples of these domains as observed in a transmission electron microscope (TEM).

1.3 Engineering importance of Fe_3Al

Interest in iron aluminides as structural materials started in the 1930s when many of its excellent properties were recognized [10, 11]. The main reasons driving the study

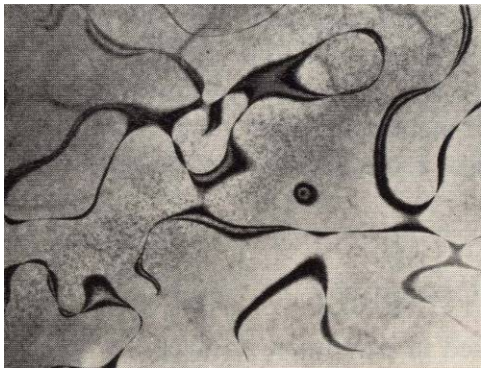

(a)

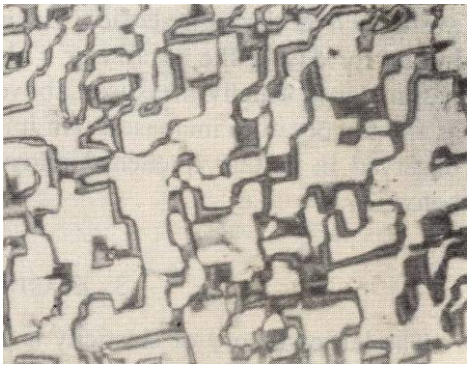

(b)

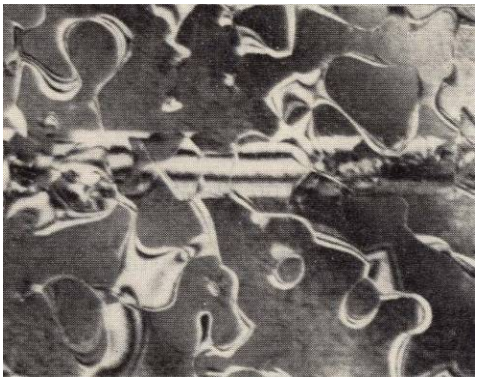

(c)

Figure 1.3 Anti phase domains observed in a TEM in (a) Fe_3Al ($D0_3$) [8] (b) Cu_3Au ($L1_2$) [12] (c) Mg_3Cd ($D0_{19}$) [13].

of iron aluminides for structural applications were the abundance and low cost of its two ingredients, iron and aluminum. As can be seen in the phase diagram (Figure 1.4) iron aluminides form a number of intermetallic phases, among which Fe_3Al and FeAl are the most interesting because of their high strength at elevated temperatures [14, 15].

Other than low material cost, iron aluminides have excellent corrosion resistance, low density (and thus good strength to weight ratio) and help conserve key strategic elements such as Cr, Ni, Mo etc.. Disadvantages of iron aluminides include low ductility at room temperature and loss in strength at elevated temperature [15-17]. Reference [18] lists some of the applications for which iron aluminides have been considered. Notable among these are jet engine compressor blades and housings, heating elements, furnace fixtures and heat exchangers.

In this study we are particularly interested in Fe_3Al based iron aluminides. Fe_3Al has been considered as an alternative to stainless steel for many applications. They are suitable for applications involving high temperature and sulphidizing and/or oxidizing environments, e.g. resistance heating elements and porous gas metal filters.

In the many extensive studies of Fe_3Al that have been undertaken by major research organizations (reviewed in [15]), the main impetus has been to improve mechanical properties through control of microstructure and composition [19, 20]. Several long-term programs on Fe_3Al were carried out at

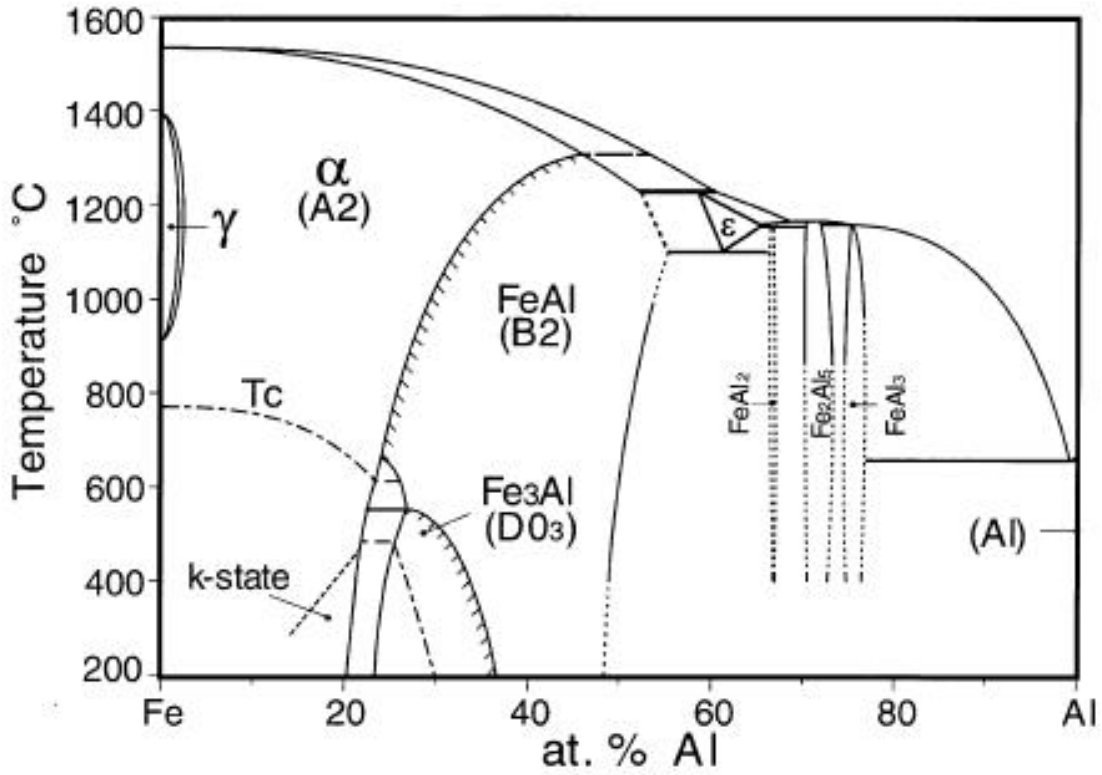

Figure 1.4 Iron-aluminum phase diagram [21].

Naval Ordinance Laboratory [18, 22-24], Ford Motor Company [25-27], Iowa State University [28-34], Pratt and Whitney [35], TRW [36], and Oak Ridge National Laboratory [19, 37-41]. These programs led to extensive characterization of Fe_3Al based alloys.

Although, a majority of these studies were aimed at improving room-temperature ductility, high-temperature strength and corrosion resistance, a number of studies, particularly references [27-32, 34, 42-45], were focused on deformation mechanisms and the study of dislocation motion, formation of anti phase boundaries (APB) and anti phase domains (APD).

These led to the discovery of some interesting properties in Fe_3Al like yield stress anomaly [46-50] and pseudoelasticity [51-54]. Although these properties cannot be exploited in engineering applications at this stage, they are very interesting from a scientific point of view.

The major part of this study is focused on the pseudoelastic effect displayed by Fe_3Al under certain conditions. As compared to other pseudoelastic materials, pseudoelasticity in Fe_3Al is unique in many respects as discussed in a later section.

1.4 Pseudoelasticity in Fe_3Al

Pseudoelasticity or superelasticty as it is sometimes called can be best described through Figure 1.5 which shows a typical stress strain curve of a pseudoelastic material. Most metals and alloys show an elastic-plastic behavior [55, 56] upon the application of

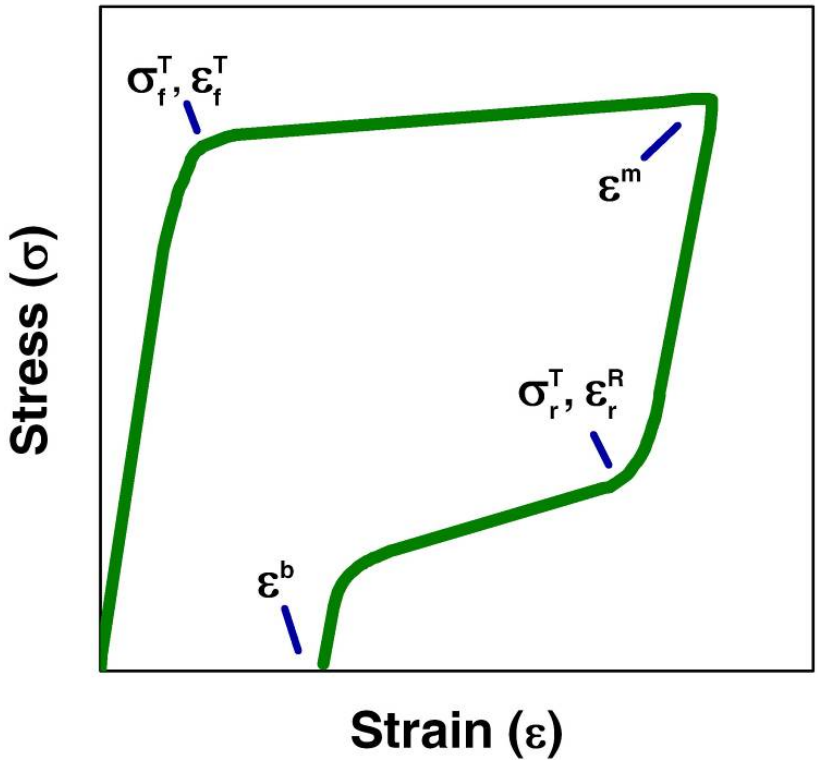

Figure 1.5 Schematic stress-strain curve of a typical pseudoelastic material.

stress, where the elastic part is the recoverable part of the applied strain and the plastic part is the non-recoverable part upon unloading. The elastic part in most crystalline metals is linear corresponding to the stretching of metallic bonds and generally accounts for a small portion of the total elongation (0.1-0.5%). The plastic part may be linear or non linear and is the result of dislocation movement (slip), twinning, or phase transformations.

In a pseudoelastic material, both the linear-elastic strain and non-elastic strain can be recovered upon unloading. The linear elastic portion is fully recovered but the non-elastic portion may be fully or partially recovered. In this text, the part of the stress-strain curve beyond the elastic limit ($\boldsymbol{\varepsilon}_f^T$) will be referred to as non-elastic, pseudoelastic or plastic whichever is appropriate. The terms pseudoelastic and plastic will be used when this part of the strain is recoverable and non-recoverable respectively. This phenomenon is commonly found in many shape memory materials and is well understood and documented [57] in those materials. The strain recovery generally occurs at a lower stress ($\boldsymbol{\sigma}_\mathbf{r}^\mathbf{T}$) than the forward non-elastic deformation stress ($\boldsymbol{\sigma}_\mathbf{f}^\mathbf{T}$). Depending on the material and testing condition, either part or all of the applied non-elastic strain may be recovered. The area under the hysterisis loop represents the amount of energy dissipated during one load-unload cycle.

In most alloys that exhibit pseudoelastic behavior e.g. NiTi [58, 59] and CuAlNi [60] a martensitic phase transformation is responsible for the effect [57]. Upon loading, the parent phase undergoes a stress-induced transformation to a martensitic phase.

Only certain twin variants of the martensite grow, that are favorably oriented with respect to the loading direction. Upon unloading the unstable martensitic phase transforms back to the parent phase thus releasing the applied strain. Martensite formation in these alloys has been confirmed using many experimental techniques including visual observation of twin variants, various diffraction techniques (X-rays [61], neutrons [62], electrons [63]), differential scanning caloriemetry [64], resistivity measurements [65], volume change etc. In addition, the martensitic phase transformation is characterized by a clicking noise upon loading and a kinking/bending during a compression test [57].

Pseudoelasticity in Fe_3Al was first reported in a series of papers by Guedou *et al.* [51-54] from 1976 to 1982. The first tests were shear tests on Fe_3Al single crystals oriented for shear on two different slip systems namely {110}<111> and {112}<111> [51]. The single crystals were heat treated to form the $D0_3$ phase (Figure 1.6) [66-68]. It was found that, for specimens of both orientations a significant portion of the applied strain was recovered upon unloading (Figure 1.7). Quenched specimens, which were expected to be α phase (BCC solid solution) did not show any strain recovery.

Also, it was found that maximum recovery occurred at a slightly off stochiometric composition Fe-23 at% Al. Shape memory effect was reported to occur at liquid nitrogen temperature. A subsequent paper [52] by the same group reported visual observations of twins and micro twins (Figure 1.8) accompanied by audible clicks during compression tests.

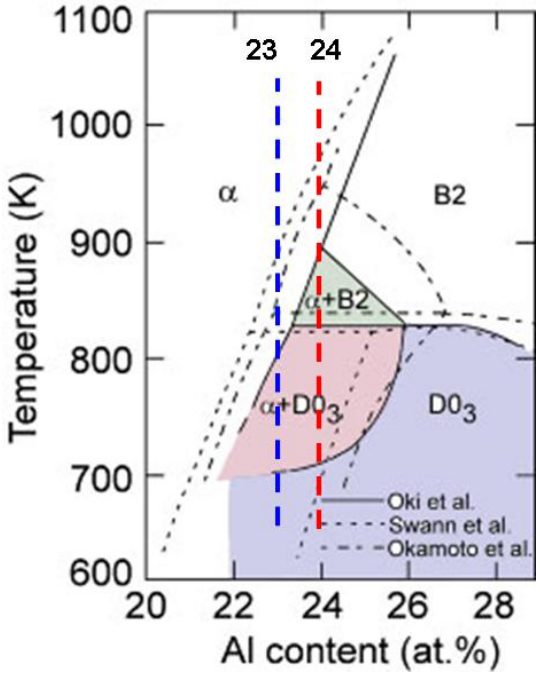

Figure 1.6 Iron-aluminum phase diagram from 20 at% Al to 28at% Al. The sequence of ordered phase changes with composition can be seen by the lines at 23% and 24 at% Al [66-68].

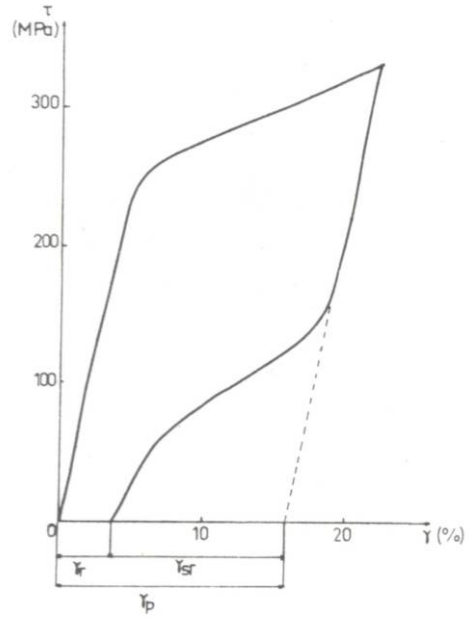

Figure 1.7 The first stress-strain curve under shear loading, showing pseudoelasticity in Fe_3Al. Guedou et al [51].

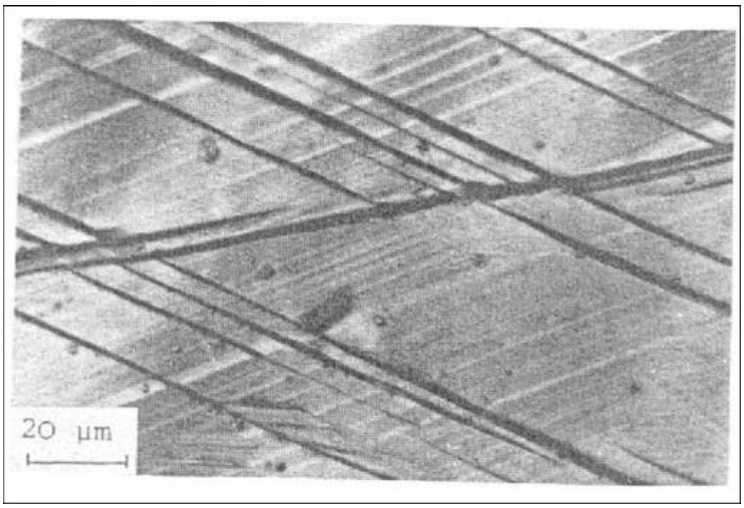

Figure 1.8 Picture of twins seen on the sample surface by Guedou et al. [52].

It was asserted that these twins were somehow related to the pseudoelastic phenomenon. Many of the above observations namely strain recovery, composition and heat treatment effects and orientation dependence were reconfirmed in later studies [69-74]. The main conclusions coming out of the above studies were that pseudoelasticity in Fe_3Al occurs only in $D0_3$-ordered single crystals (it was later also reported in textured polycrystalline Fe_3Al by Nosova et al.[71]), and the amount of recovery depends on the orientation of the crystal with respect to the loading direction.

In a later paper [54] from the same group which discovered pseudoelasticity in Fe_3Al, a model based on TEM observations was proposed to explain the phenomenon. Dislocation configurations and their motion were studied in thin foil specimens under tensile load, in a TEM. The model was based on movement of APBs on certain crystallographic planes. The APB surface tension was thought to be responsible for providing the reverse force for strain recovery. This mechanism is discussed in detail in a

later section. The idea of twins and/or phase transformation as the responsible mechanism was rejected by Kubin et al. [54].

A number of other papers [69, 70, 74] have supported these observations. Their interpretations differ slightly but follow the same broad theme. Kubin et al. [54] also mentioned that no evidence of martensite was found during resistivity measurements and dilatometry experiments but did not provide any details of those experiments. The recovery in compression as a function of orientation as reported by Yasuda et. al. [73] is summarized in Figure 1.9. It is important to mention here that orientation studies showed some ambiguity because pseudoelasticity was maximized for an unexpected orientation. The traces found on the specimen were those of the {112} planes, and {112} <111> type twins are known to exist in $D0_3$ ordered Fe_3Al [75]. But, specimens oriented ideally for these twins show less strain recovery in compression than those oriented to maximize {110} <111> slip. This was the main reason why twinning was not investigated further in any of these studies.

None of the above studies involved detailed *in situ* or *ex situ* diffraction experiments on the single crystals. Kubin et al. [54] mentioned cursorily that Laue diffraction patterns do not show any change during and after loading.

To summarize, pseudoelasticity is strongly influenced by the orientation of the crystals. Crystals aligned for maximum resolved shear stress on the {110} <111> slip system recover the maximum amount of applied strain. The composition at which pseudoelasticity is maximized is Fe 23 at% Al. Strain recovery occurs only in the $D0_3$

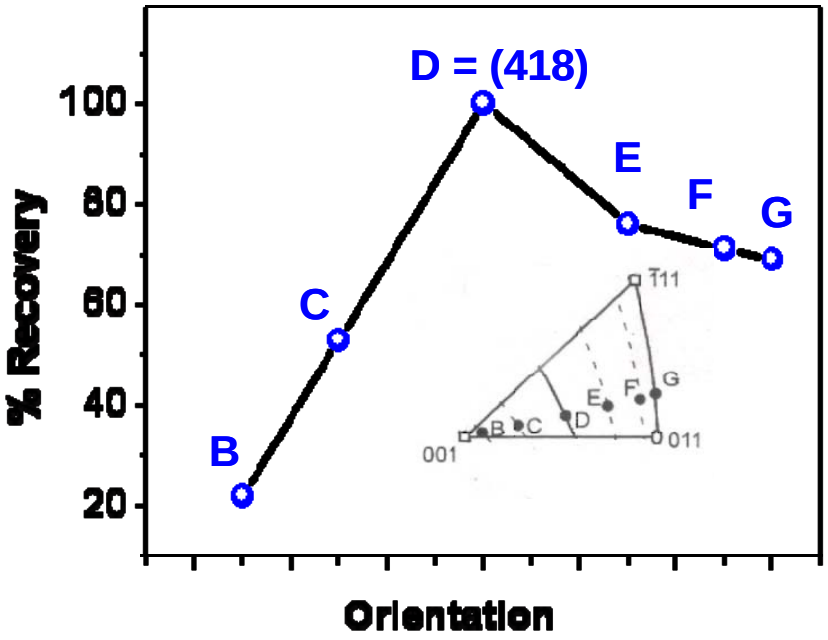

Figure 1.9 Orientation dependence of pseudoelastic recovery upon compressive loading[73].

phase and not in the B2 or solid solution (α) phases which also exist in the same composition range. None of the studies found any evidence of a phase transformation and there were conflicting reports on the presence of twins. The only explanation suggested for this effect so far is that the surface tension of the APB formed during deformation provides the reverse force for strain recovery. Therefore, there is a need to revisit this effect and investigate the mechanism in more detail. There are three different possible mechanisms that could be responsible for the pseudoelastic effect in Fe_3Al. These are discussed in the following section.

1.4.1 Possible mechanisms

(a) Surface tension of APBs

Anti phase boundaries (APBs) are boundaries which separate two different ordered regions of an ordered lattice. As will be explained in detail below, the two regions on either side of an APB have the same ordered structure but the order is disrupted across the APB itself. APBs may be formed by passing partial dislocations through an ordered lattice. As a simple example Figure 1.10 shows the formation of an APB in a B2 ordered lattice. All the planes shown in the figure are {110} planes, 1.10 (a) and 1.10 (b) represent a BCC lattice and 1.10 (c) and 1.10 (d) the B2 lattice. If a ½<111> dislocation moves through region 1, the BCC planes remain unchanged (Figure 1.10 (b)) since there is only one type of atom. However, as can be seen in Figure 1.10 (d), after the passage of a ½ <111> dislocation in the B2 lattice, although regions 1 and 2 retain the

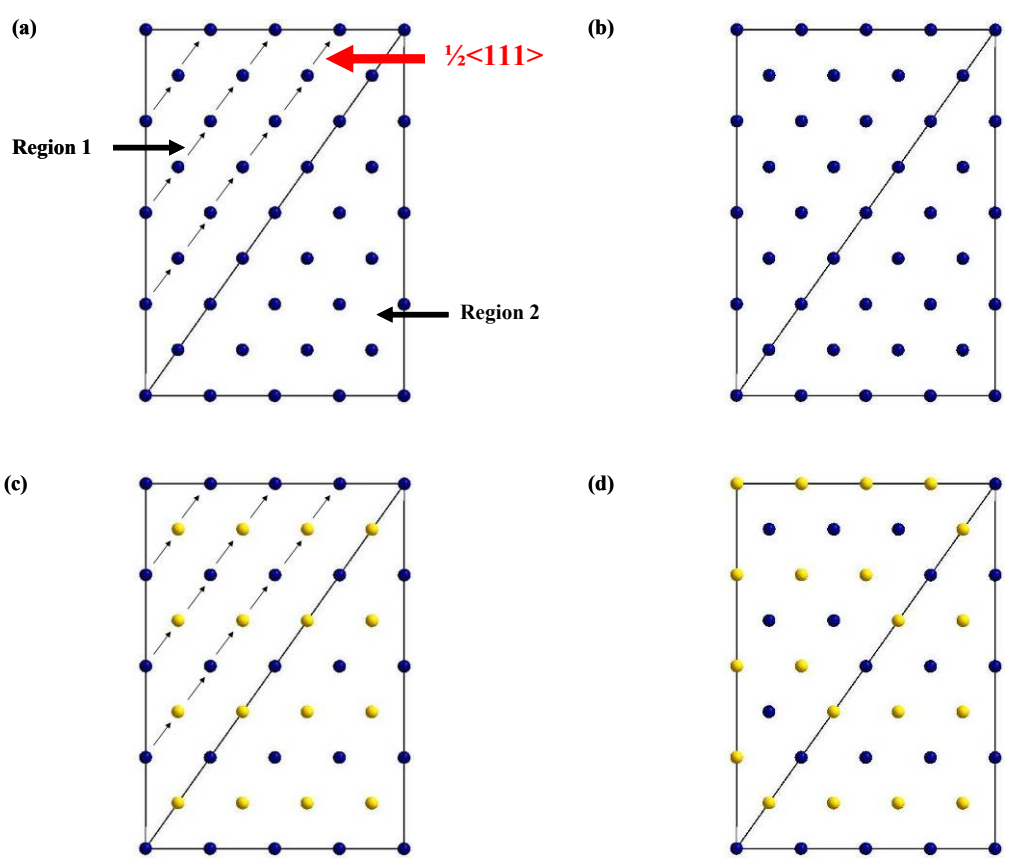

Figure 1.10 Formation of antiphase boundaries (APBs). (a) represents {110} planes of a BCC lattice. Upon passing a ½<111> dislocation through region 1 the overall lattice remains the same as seen in (b). (c) shows the {110} planes of an ordered B2 lattice. Passing a ½<111> dislocation produces an APB between regions 1 and 2 as seen in (d).

same order, the boundary between the two regions has wrong nearest neighbor bonds and is, therefore, an anti phase boundary (APB). If we consider an expanding dislocation loop, the area contained within this loop will act as an APB between the two ordered regions (volumes) on either side of this area. If another ½<111> dislocation is passed through region 1 in Figure 1.10 (d) it would eliminate the APB.

The $D0_3$ lattice (Figure 1.11) is also based on the BCC lattice but is more complicated than the B2 ordered structure. The lattice can be described by 2 x 2 x 2 BCC type cells. In a $D0_3$ ordered Fe_3Al unit cell, all the corner positions and four of the body centre positions are occupied by Fe atoms. Aluminum sits on the remaining four body centers. The conventional indicial notation for the $D0_3$ structure is based on the unit cell shown in Figure 1.11 and will be used throughout this text. However, in some papers e.g. Kubin et al. [54] indices based on a single BCC unit cell have been used.

Analogous to the ½ <111> dislocation on the {110} plane of the B2 lattice described above, the $D0_3$ <111> dislocation consists of 4 partials. That is, the first partial is ¼ <111> the second is ½ <111> and so on. As a result of the 4 partials there are 2 types of APBs that can form upon passage of the <111> partials.

The APB mechanism to explain pseudoelasticity in Fe_3Al was proposed on the basis of TEM observations of dislocation motion seen in thin foil specimens under tension [54].

These qualitative observations were coupled with approximate energy calculations to come up with the model. In essence, the model states that the <111>

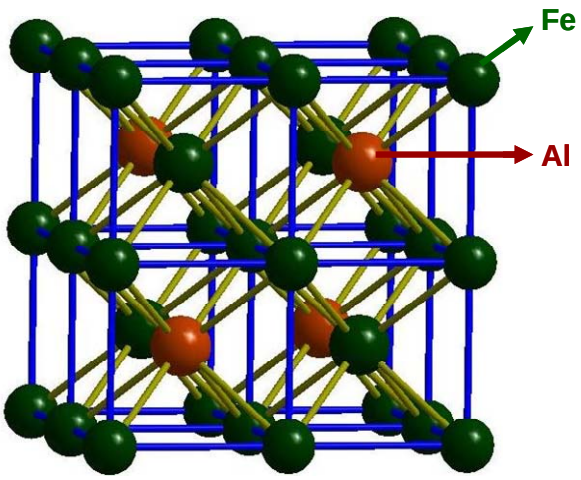

Figure 1.11 Ordered $D0_3$ lattice. Green spheres represent Fe atoms and red spheres Al atoms.

partials move relative to each other extending the APBs on the {110} planes. The surface tension of these APBs is the driving force for strain reversal.

Recently, Yasuda et al. [69] have published a more detailed account of the movement of dislocations. Their model can be explained with the help of Figure 1.12. According to Yasuda et al. [69], when a load is applied to the sample, the first superpartial namely ¼ <111> moves faster than the remaining 3 superpartials on the {110} plane, thus dragging an APB between itself and the remaining partials. This APB region has some surface tension associated with it. Upon unloading this superpartial springs back owing to the surface tension of the APB and restores the applied strain.

In addition to the APBs formed by movement of superpartials, there are other APBs in an ordered single crystal because of the existence of domain structure. Ordered domains in a single crystal can be thought of as grains inside a polycrystalline material.

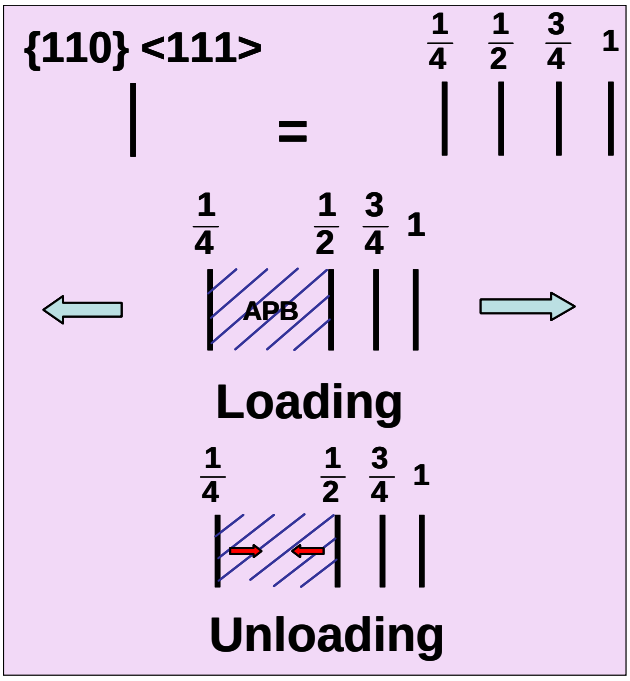

Figure 1.12 APB mechanism as proposed by Yasuda et al. [69]

Unlike polycrystalline grains, ordered domains do not differ in crystallographic orientation but only in order.

For example, two neighboring domains would be a part of the same lattice and have the same type of order (e.g. $D0_3$) but would have an APB between them so that the stacking sequence changes across this boundary. As a one dimensional example Figure 1.13 shows an ordered structure on either side of the dashed line. The ordering is ABC on either side of the line. Across the line however wrong nearest-neighbor bonds are present.

The dashed line represents an APB in a one dimensional system. In this structure there are a number of different APBs that can form e.g. AA, BB, and BA. In Figure 1.13 the APB formed is a CC type. Similarly, at an ordered domain boundary there are different types of APBs that can form on different planes. For example, on the {110} planes there are 2 types of APBs as mentioned above (dislocation induced APBs).

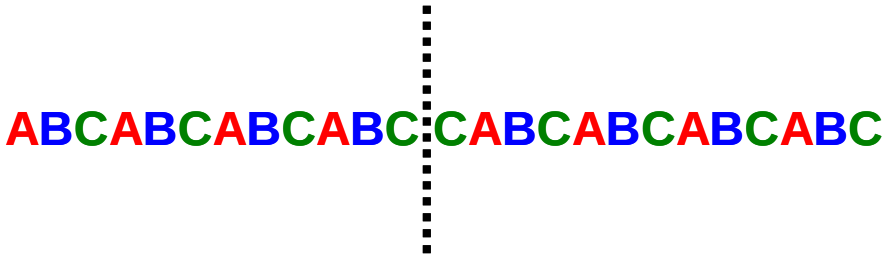

Figure 1.13 Two ordered domains separated by an APB in a one dimensional ordered system.

In the mechanism described above we have ignored the presence of ordered domains. That is, we have assumed that superpartial dislocations move within one ordered domain. Yasuda et al. [69] have discussed what happens when different types of superpartials cross an ordered domain. Such events could move the domain boundaries and thus change domain sizes which could expand or shrink depending on which type of partial crosses which type of domain boundary. They assert that pseudoelasticity is closely related to domain size. The details of these effects are not described here but can be found in [69].

(b) Martensitic Phase Transformation

Stress induced martensitic phase transformation is responsible for pseudoelasticity in many ordered alloys [57] most notably in NiTi and CuNiAl which have been extensively studied. The martensitic transformation and the nature of the resulting martensite are discussed first followed by its role in pseudoelasticity. Martensitic transformation is a phase transformation which occurs by a cooperative motion of several atoms upon application of a shear stress. There is no diffusion involved in this kind of phase transformation. The parent phase is usually a cubic lattice which transforms into a crystal structure of lower symmetry. Consequently, many different martensite variants can form depending on the transformation conditions. Figure 1.14 (a) shows a simplified picture of two martensite variants A and B that form in response to shear on the planes represented by the dashed lines. These martensite variants are often twin variants of each

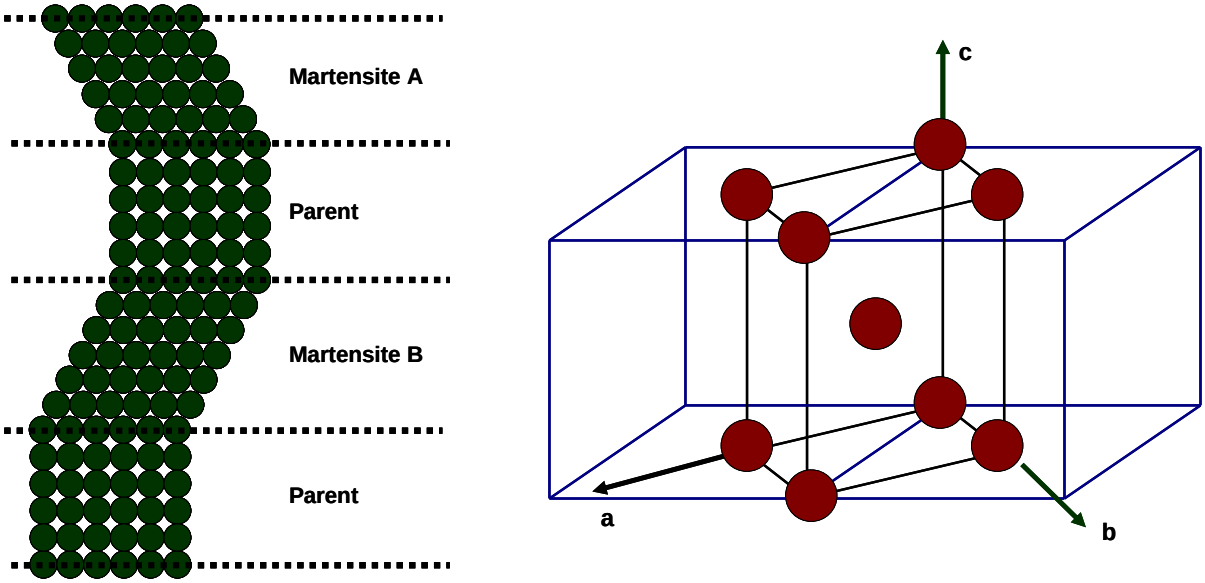

Figure 1.14 (a) Two dimensional representation of martensite variants A and B from a cubic parent phase. (b) FCC-BCT transformation in steel as proposed by Bain [76].

other. A typical example of the structure resulting from such a transformation is shown in Figure 1.14 (b) which shows a face centered cubic to body centered tetragonal transformation in steels. The blue lines represent the parent phase which is a FCC lattice. This structure can easily be transformed into a BCT structure by expanding along the *a* axis of the BCT cell and contracting the *c* axis such that *c/a* ratio becomes close to one.

When the shear stress reaches a critical level on certain crystallographic planes upon application of load the parent transforms to a martensitic phase. In a pseudoelastic material, the martensite becomes unstable upon removal of the load and transforms back to the parent phase, thus reversing the applied strain. There is no permanent slip since the martensitic transformation in such alloys takes place at a lower stress level than that required for slip.

The stress-strain curve of single crystal Fe_3Al (Figure 1.7) is very similar to those of known pseudoelastic materials like NiTi, CuAlNi etc. Since martensitic phase transformation is the most common known reason for pseudoelasticity, there is a need to look for phase transformation in Fe_3Al upon loading.

(c) Twinning

Twins are similar to the martensitic transformations described in the preceding section. In both cases a finite volume of the parent crystal realigns itself to form a new lattice. Unlike martensite, twins have the exact same crystal structure as the parent phase differing only in their crystallographic orientation. There are two types of twins, growth twins and deformation twins. In this section we are only interested in deformation twins. Analogous to martensite formation, deformation twins are formed due to a shear on

certain crystallographic directions. Figure 1.15 illustrates twin formation when a shear stress acts on the twinning planes represented by the dashed lines. Note that each plane moves only a small distance relative to the preceding plane but the overall displacement is quite significant. Oval shaped atoms have been used to clearly illustrate the change in crystallographic orientation. The direction indicated by the green arrow in the parent crystal has to undergo a large rotation before it lines up along the direction shown by the red arrow in the new twinned crystal.

Twins are the preferred deformation mode at low temperatures and in crystals with low symmetry. These are conditions when slip becomes difficult either due to lack of vibrational energy (at low temperature) or lack of available slip systems (in low symmetry crystals). Under these conditions twins become energetically favorable and can form at lower stresses than those required for slip. Twins have the same crystal structure as the parent lattice and therefore do not have any stored chemical energy. They are stable under the conditions that the parent is stable. So, the question is whether these twins could provide the reverse force required for pseudoelasticity. Although there is no chemical energy stored in twins there is some elastic energy that is stored in the crystal to accommodate certain types of twins. This is illustrated using Figure 1.16, which shows a single twin variant in a compressed sample where the twins run from one free surface to the other without running into the compression platens. These twins do not have any chemical or elastic energy stored in them and therefore do not have any driving force to de-twin. Figure 1.16 (b) shows another case, where several twins variants run into the

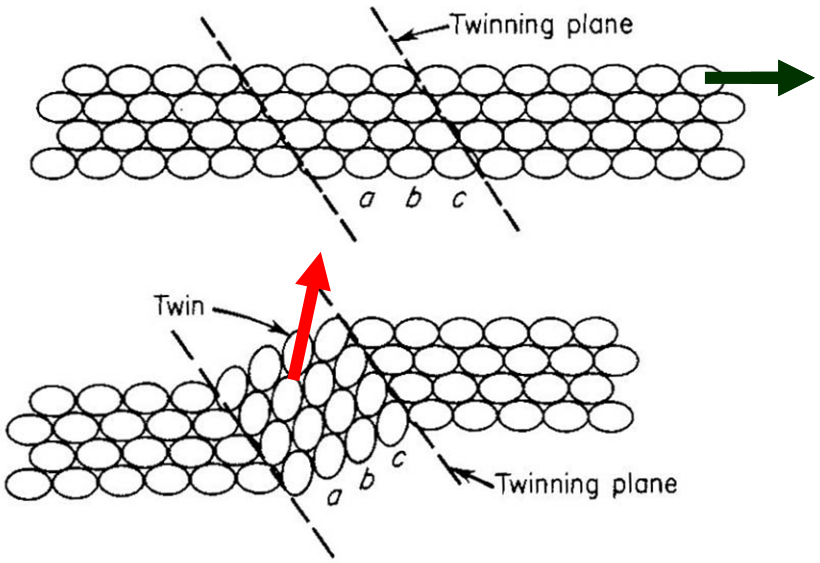

Figure 1.15 Schematic illustration of deformation twin [77].

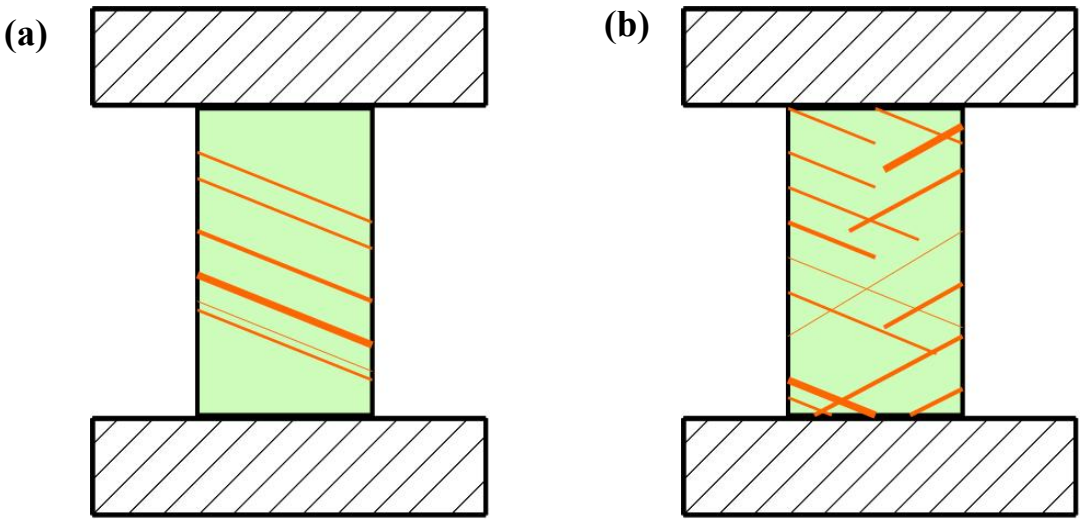

Figure 1.16 Comparison of (a) twins running from one free surface to another free surface and (b) elastically accommodated twins.

compression platens and do not cross the width of the entire sample. These twins are accommodated by elastic deformation of the surrounding untwined regions. Once the load is released the stored elastic energy forces the twin to transform back to the original state.

Although there could be many twinning systems in theory, only a few are preferred by real crystals e.g. in BCC crystals the normal twinning plane is {112} and the twinning direction is <111> (details of twinning crystallography can be found in reference [78]). If a pure metal (e.g. Fe) twins in the above sense the resulting structure is identical to the parent structure. However, if an ordered alloy like Fe_3Al twins in the above sense, the resulting structure has the same lattice as the parent but the order is changed i.e. the atoms which were originally sitting at certain lattice points are no longer in the same positions. This is seen in Figure 1.17 where the order in the crystallographic direction indicated by the green arrow is ABAB or XYXY in the parent crystal. After the twinning operation the red arrow indicates the same crystallographic direction in the twinned part. The order in this direction is now AYBX in each layer. Nevertheless, the resulting structure is still ordered. These kinds of twins are known as pseudotwins. In the strict sense pseudotwins are a different phase than the parent phase. Pseudotwins have been reported by Green and Cohen [79] in $D0_3$-ordered Fe_3Be. Its pseudoelasticity has been attributed to pseudotwinning (with {112} twin plane and <111> twin direction) [79]. Since the order in pseudotwins is not the same as the parent (which is the most stable order at that temperature), pseudotwins also have some chemical free energy. Therefore, there are two types of energies which drive the restoring force for reversal of

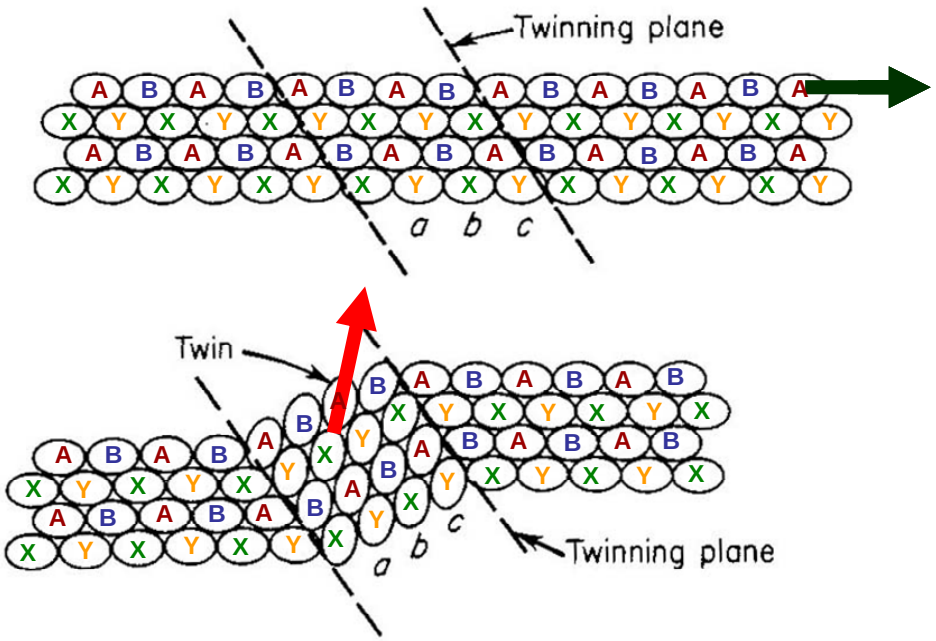

Figure 1.17 Formation of a pseudotwin accompanied by a change in order.

applied strain, namely the chemical energy due to unstable ordering of the pseudotwins and the elastic energy in the untwined regions of the crystal to accommodate these twins.

Chapter # 2

Experimental Methods

The experimental procedures employed in this work can be divided into three broad categories which are alloy preparation (casting, thermo-mechanical processing and single crystal growth), mechanical testing procedures and neutron diffraction experiments. Among these the first two will be described here. The details of the neutron diffraction experiments have been included in chapter 4 for the sake of continuity.

2.1 Alloy preparation

2.1.1 Arc melting

Several Fe_3Al and FeCo alloys were arc melted and drop cast in a cylindrical copper mold measuring 13 mm in diameter for Fe_3Al and 130 mm length. Figure 2.1 shows a picture of the water cooled melting hearth in the main chamber of the arc melter. Figure 2.2 shows a photograph of the copper molds and Fe_3Al cast rods used in this study. The iron and aluminum starting materials (>99.99% pure) were carefully weighed and then mixed by arc melting, with the buttons flipped and re-melted five times to ensure good mixing before drop casting. Total weight losses after

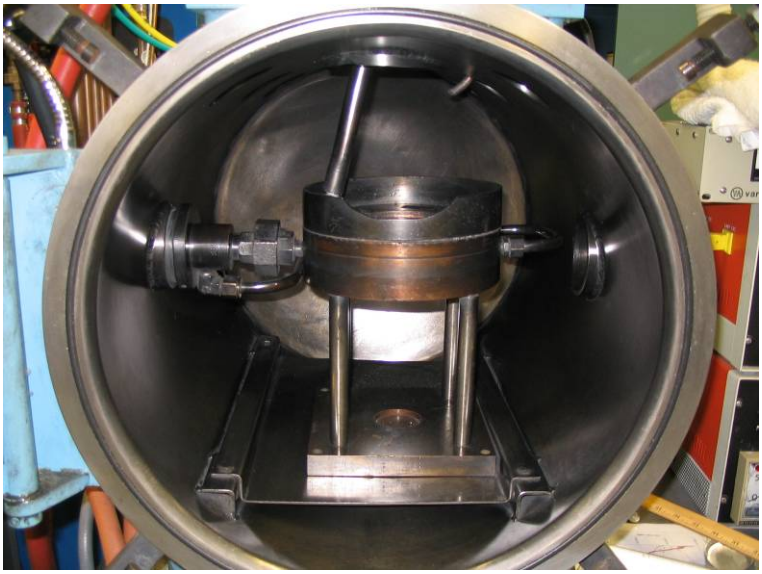

Figure 2.1 The inside of the arc melter chamber. The water cooled jacket in the middle holds the molds. Also seen is the arcing rod.

Figure 2.2 Copper molds and cast Fe_3Al rods.

melting and casting were less than 0.1%, which led to negligible changes in alloy composition after melting. Therefore, all compositions discussed in this paper are nominal compositions (atomic %) unless otherwise stated.

2.1.2 Growth of single crystalline Fe_3Al

The cast alloys were directionally solidified in an optical zone melting furnace (Figure 2.3) at a growth rate of 40 mm/h to obtain single crystals (Figure 2.4). During growth of the first single crystal, a polycrystalline rod was used as a seed and the diameter of the molten zone was carefully reduced to produce a neck that prevented the slower growing grains from propagating.

This produced a single crystal with growth direction <100>, as determined by Laue back scattered X-ray diffraction. As is explained by the schematic in Figure 2.5, this single crystal was reoriented and cut normal to the <418> direction and used as seed to produce additional single crystals with the <418> growth direction. This allowed us to obtain large samples in the <418> direction. The quality of single crystals was examined by Laue back scattered X-ray diffraction after every growth. Only those single crystals with high quality were used for further examination.

2.1.3 Heat treatments

The Fe_3Al single crystals were homogenised at 1100 ^oC for 48 h, followed by furnace cooling at 80°C/h to ensure $D0_3$ order, as described in reference [68].

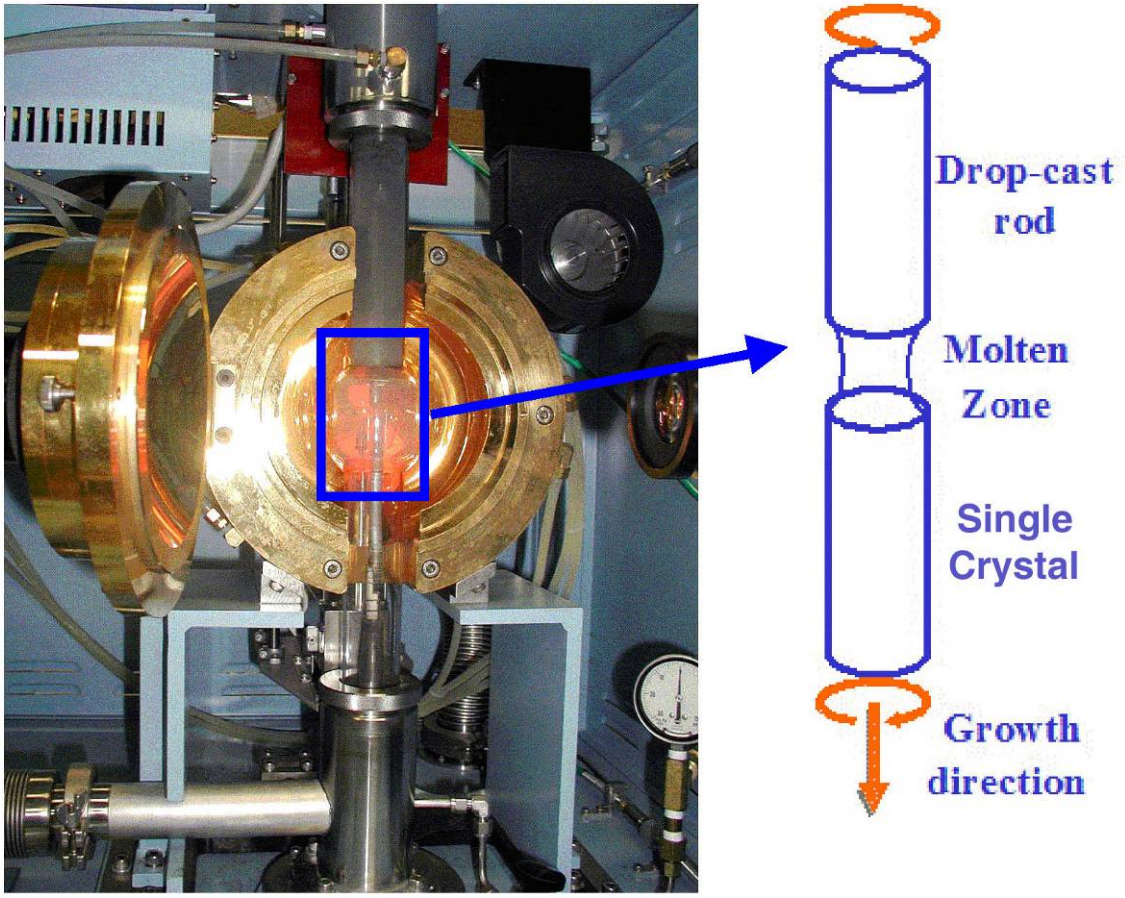

Figure 2.3 The optical zone melting furnace. Schematic diagram shows the single crystal growth process.

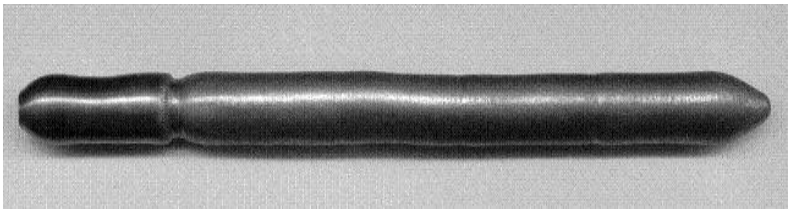

Figure 2.4 Picture of grown single crystal Fe_3Al rod.

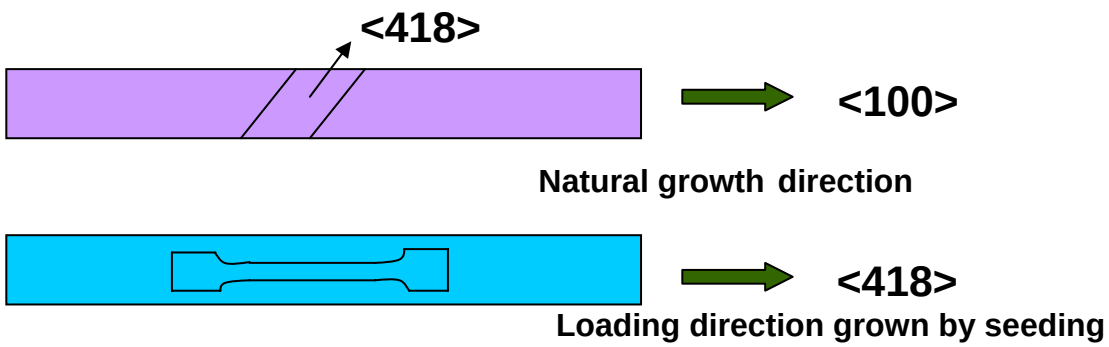

Figure 2.5 Schematic of seeding procedure used to grow single crystals in the <418> direction.

2.2 Mechanical testing

2.2.1 Sample preparation

The as grown single crystal Fe_3Al rod was mounted on a two-angle goniometer (Figure 2.6) and a Laue X-ray measurement was done on the sample. The goniometer angles were adjusted to get exactly the desired orientation perpendicular to the goniometer face. The goniometer was then mounted on an EDM (electrical discharge machine) and samples were cut. Several different geometries of tensile and compression samples (Figure 2.7) were cut. The orientations of the final samples were found to be within 1^o of the desired orientation. These samples were then ground (upto 1200 grit paper) and polished (alumina powder) to remove any non-uniformity.

2.2.2 Uniaxial tests

Several different tensile and compression tests were carried out in various load frames. Three different load frames, two made by Instron® and one by MTS® were used

Figure 2.6 The two angle goniometer used to orient single crystal samples.

Figure 2.7 Various geometries of tensile and compression samples.

for these tests. Strain measurement was carried out using an extensometer in certain cases. High temperature mechanical tests were carried out in a furnace mounted on the load frame. For low temperature tests two different methods were used. Some tests were done in various dry ice baths (which stabilize at known temperatures) and other by flowing liquid nitrogen through a copper tube surrounding the sample.

Tensile tests on single crystal Fe_3Al were always done on flat dogbone shaped specimen with a universal joint in the load train to avoid any alignment problems. For surface observations small samples were loaded in a tensile rig specially fabricated for this purpose (Figure 2.8). For both Fe_3Al and FeCo compression sample geometries were either cylindrical or cuboidal.

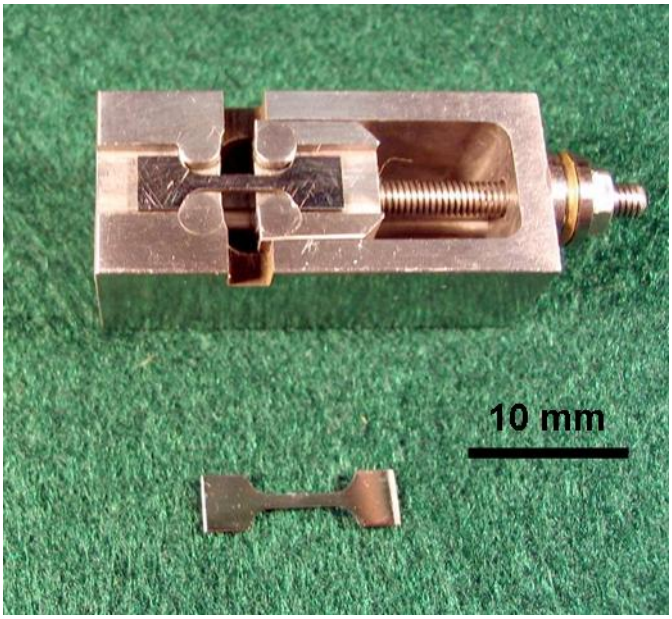

Figure 2.8 Tensile rig for loading small polished samples for surface observations.

Chapter # 3

Mechanical Properties of Pseudoelastic Fe_3Al

In this chapter a quantitative description of the pseudoelastic effect in Fe_3Al is given. The macroscopic room temperature response of single crystal Fe_3Al under tension and compression is described in the first section. This is followed by the mechanical response of Fe_3Al at temperatures higher and lower than room temperature, including the shape memory effect shown by this material at very low temperatures. Also, surface features appearing on the samples during mechanical loading are described in this chapter.

3.1 Stress-strain response at room temperature

As was explained in chapter 1, unlike many other well known pseudoelastic materials, Fe_3Al shows pseudoelasticity only in the single crystal form and in certain crystallographic directions. The pseudoelastic effect in Fe_3Al is maximized when the single crystal is uniaxially loaded in the <418> direction[73]. Therefore in the present chapter all mechanical tests have been done in the <418> direction. Certain other directions were used in some experiments (in chapter 4) but unless otherwise stated <418> was the direction used for all uniaxial mechanical loading.

Figure 3.1 shows stress strain curves of <418> oriented Fe_3Al single crystals under tensile and compressive loading, displaying the pseudo-elastic behavior of this alloy. The samples were loaded to 4% and 3% total strains, respectively, and subsequently unloaded. The strain recovery occurs at a very low stress (~100-200 MPa), thus making an unusually big hysterisis loop. There is a tension-compression asymmetry in the material. The stress at the elastic limit under compression is ~ 40MPa higher than in tension. When cycled a second time through the load-unload cycle in tension, the specimen broke between 2 to 4 % while loading (Figure 3.2). Also, the material strain hardens continuously during compression but does not in tension even at strains as high as 13% (Figure 3.3(a)).

Figure 3.3 (a) and 3.3 (b) show the amount of recovery in tension and compression for various applied strains. The strain on the tensile curves (Figure 3.3 (a)) were obtained from extensometer readings, but for compression tests (Figure 3.3(b)) strains were calculated from corrected crosshead positions. It was found that up to 10% strain can be almost fully recovered in tension. When specimens were strained more than 10%, a significant part of this strain was not recovered upon unloading. At 13% applied strain ~9% strain remained as plastic strain upon unloading. In compression (Figure. 3.3(b)), there is less recovery. The amount of unrecovered strain becomes significant in the applied strain range of 9-10 %.

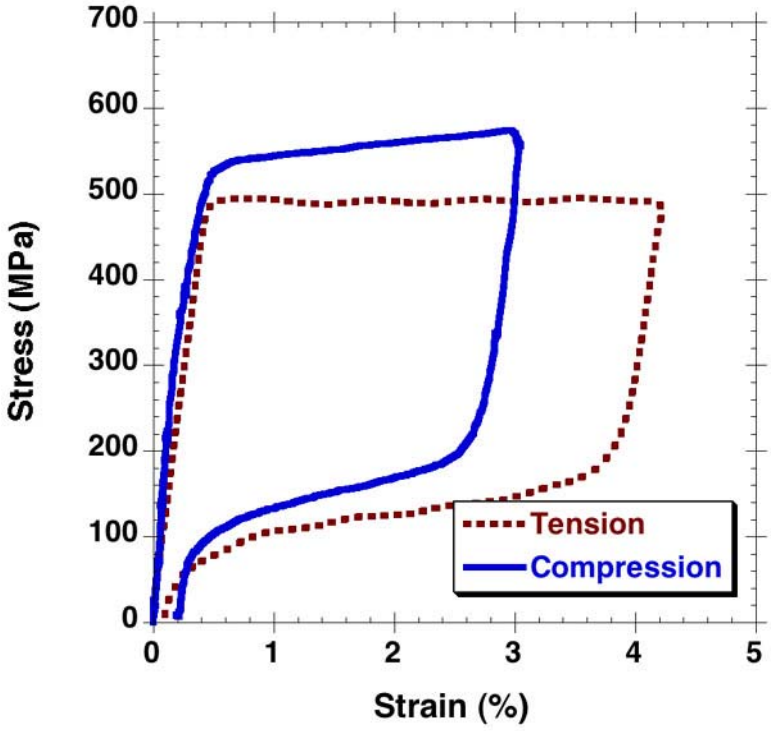

Figure 3.1 Stress-Strain curves of single crystal Fe_3Al in <418> direction in tension and compression.

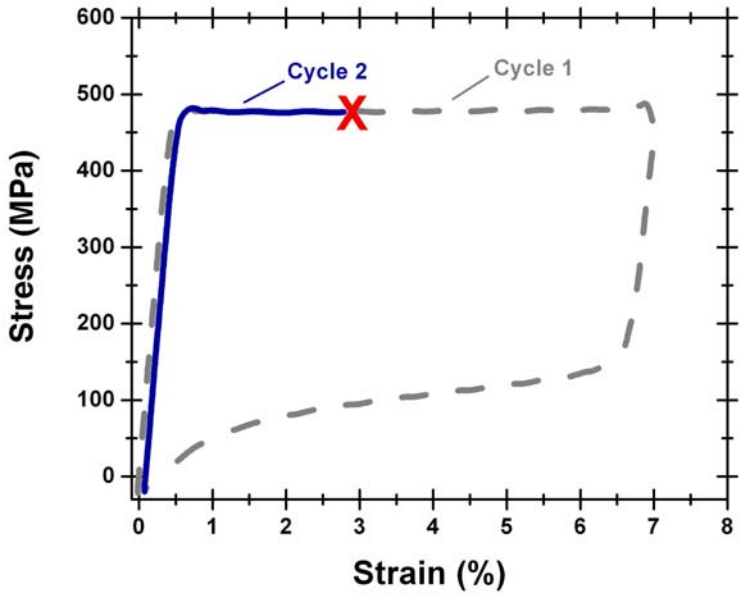

Figure 3.2 Tensile stress-strain curves of specimen cycled twice in tension. Red cross shows the fracture in the 2nd cycle.

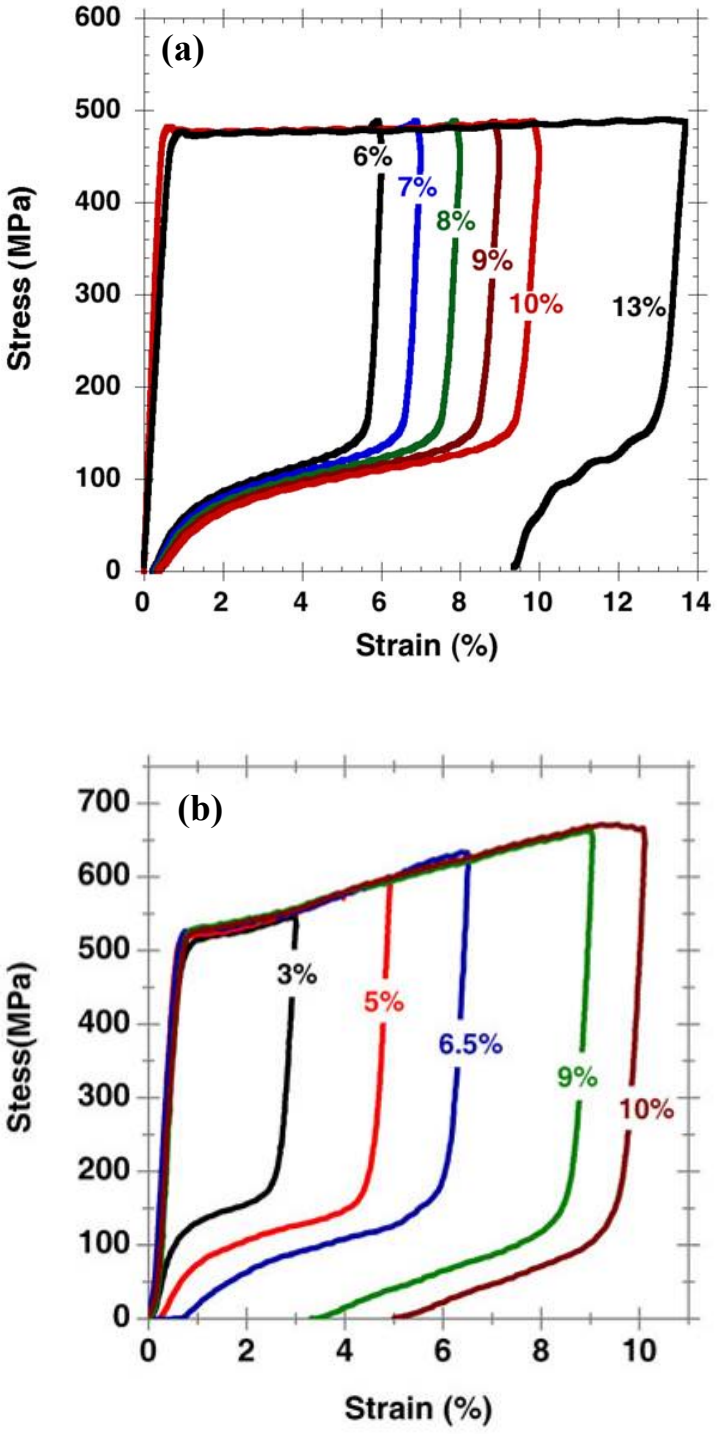

Figure 3.3 (a) Tensile stress-strain curves of monocrystalline Fe_3Al showing different amounts of recovery when unloaded from different strains. (b) Compressive stress-strain curves of monocrystalline Fe_3Al unloaded from various applied strains.

In samples which were strained up to 10% in tension, a small portion of the applied strain (~3% of total) was not recovered immediately. Rather recovery occurred as a function of time as shown in Figure 3.4. The amount of unrecovered strain increased with increasing applied strain. The recovery with time followed an exponential curve.

The surfaces of tensile samples were observed during tests and two types of surface steps were found at different strain levels. One of these were shown to be traces of the (211) planes. These results have been discussed in detail in the discussions section.

3.2 Stress-strain response at high temperature (100 -140 ^{o}C)

Figure 3.5 summarizes the stress-strain response observed between room temperature and 140 ^{o}C. High temperature tensile tests showed that pseudo-elastic behavior persisted up to a temperature of 100^{o}C. At 120^{o}C, although there was some pseudoelastic recovery, the sample did not recover most of the applied strain. At even higher temperature (140^{o}C), the material deformed plastically without any recovery except the elastic part. At these higher temperatures, a very small stress drop occurred during loading in the previously flat (at room temperature) pseudo-elastic region of the stress strain curve (at a peak stress of ~500 MPa). The plateau stress wavered by a small amount (Figure 3.6) indicating that possibly two different deformation mechanism were active at 120^{o}C namely one responsible for the slight pseudo-elasticity and the other responsible for the plasticity.

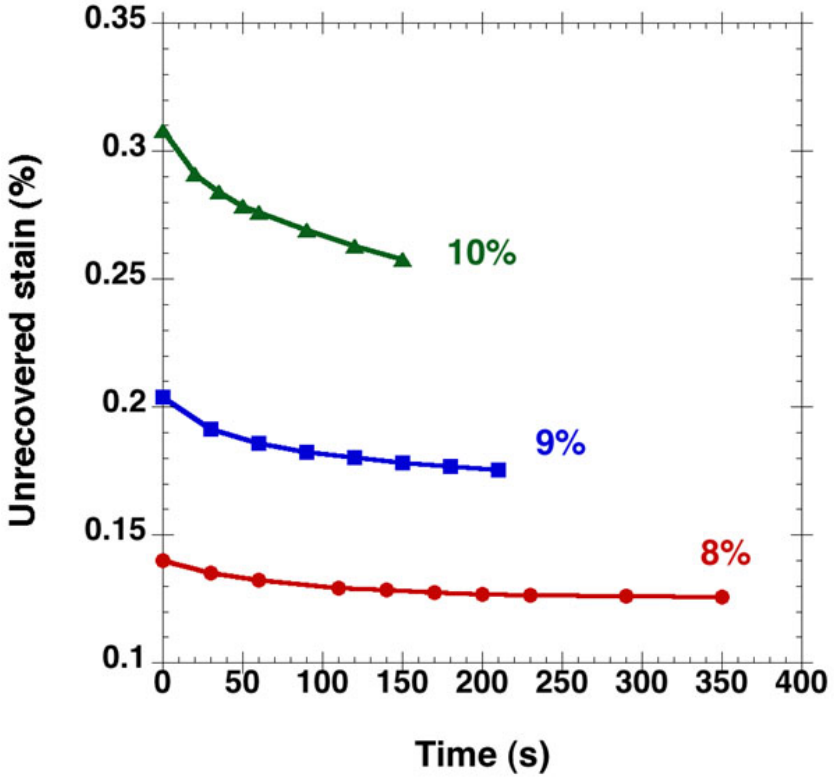

Figure 3.4 Strain recovery as a function of time for three different applied maximum strains.

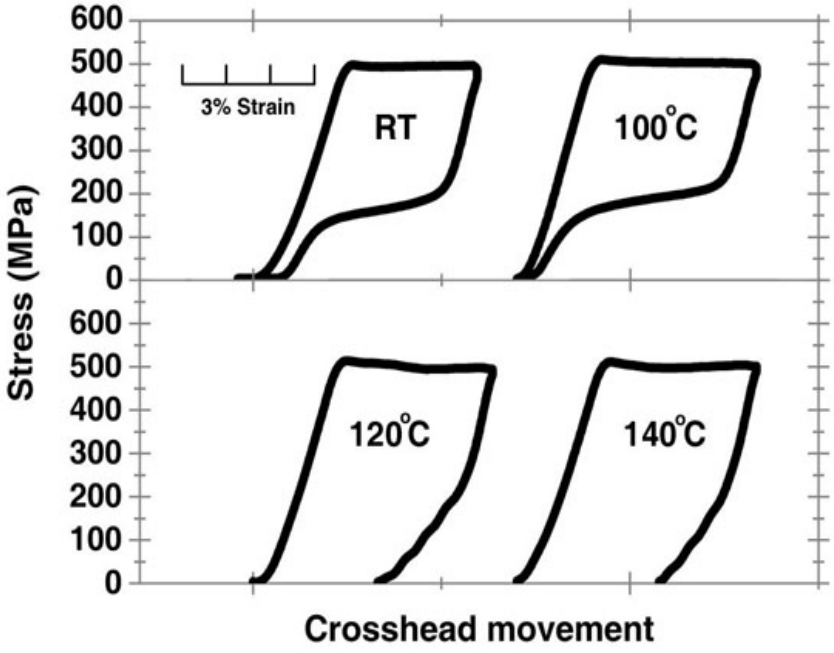

Figure 3.5 Tensile stress-strain curves of monocrystalline Fe_3Al at room temperature and above.

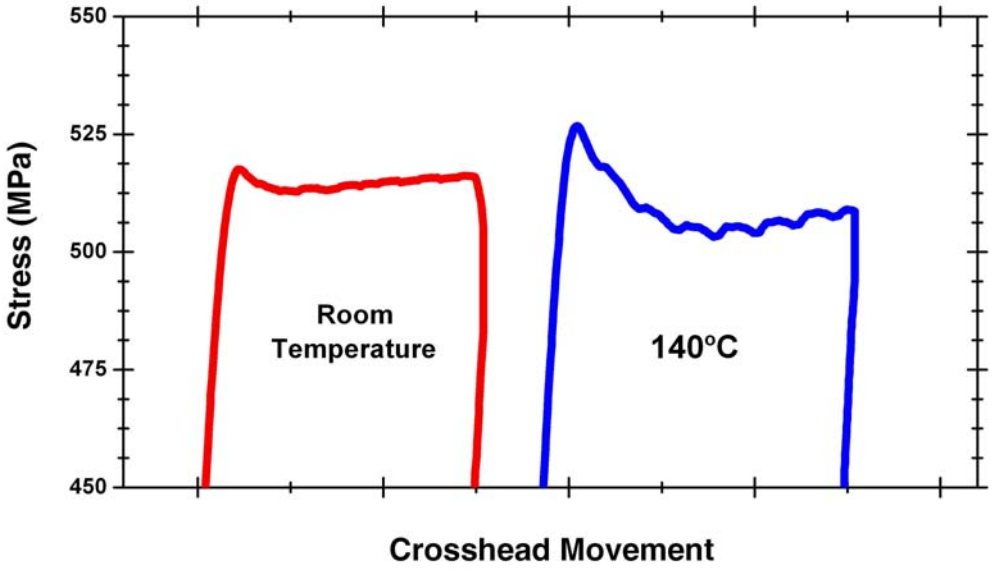

Figure 3.6 Expanded view of the upper part of the stress-strain curve of monocrystalline Fe_3Al at room temperature and 140°C.

3.3 Stress-strain response at low temperature (-196 ^{o}C to room temperature)

Tensile tests were carried out in various low temperature baths using dry ice and liquid nitrogen. As seen in Figure 3.7, up to a temperature of -73^{o}C, the applied strain of ~3% was fully recovered. At liquid nitrogen temperature (-196^{o}C) none of the applied strain (~1%) was recovered. Furthermore, the stress at the elastic limit was significantly higher than at room temperature and other low temperature tests. All of this strain was recovered after the sample was heated up to room temperature, thus displaying the shape memory effect, which was observed both in tension and compression. Unlike well known shape memory alloys like NiTi alloys, Fe_3Al showed the shape memory effect only at very low temperatures. Another sample was compressed to ~2.5% strain at a temperature of -178^{o}C. Only the elastic part of the strain was recovered upon unloading. The controls were then shifted to constant load control and a small load corresponding to a stress of ~15 MPa was applied to hold the sample in place. The sample was allowed to slowly heat up to room temperature. The crosshead movement was monitored as a function of temperature, as shown in Figure 3.8. Two distinct slopes were seen on the plot of crosshead position vs. temperature. The first one corresponds to the thermal expansion of the sample and the grips. The second slope is a superposition of the thermal expansion and the strain recovery upon heating up. The two straight line curves intersect at ~ -143^{o}C, which is the temperature at which recovery commences.

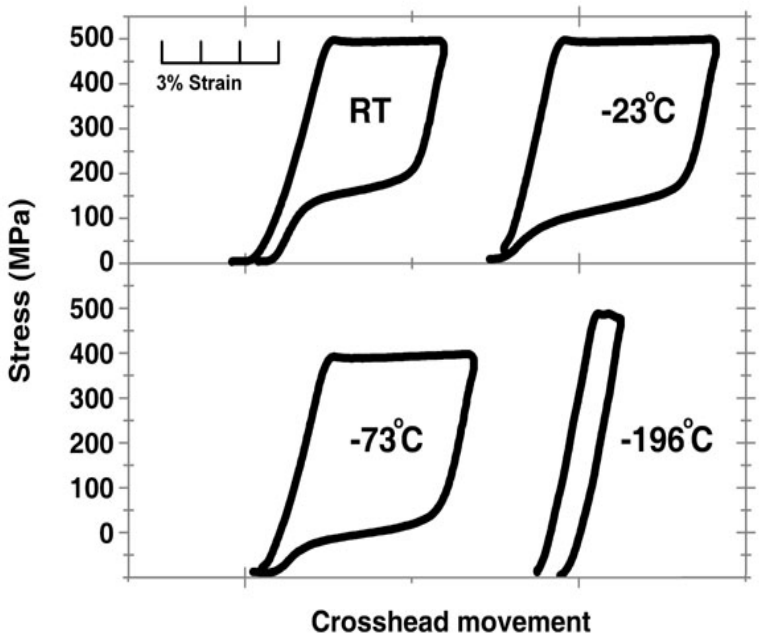

Figure 3.7 Tensile stress-strain curves of monocrystalline Fe_3Al at room temperature and below.

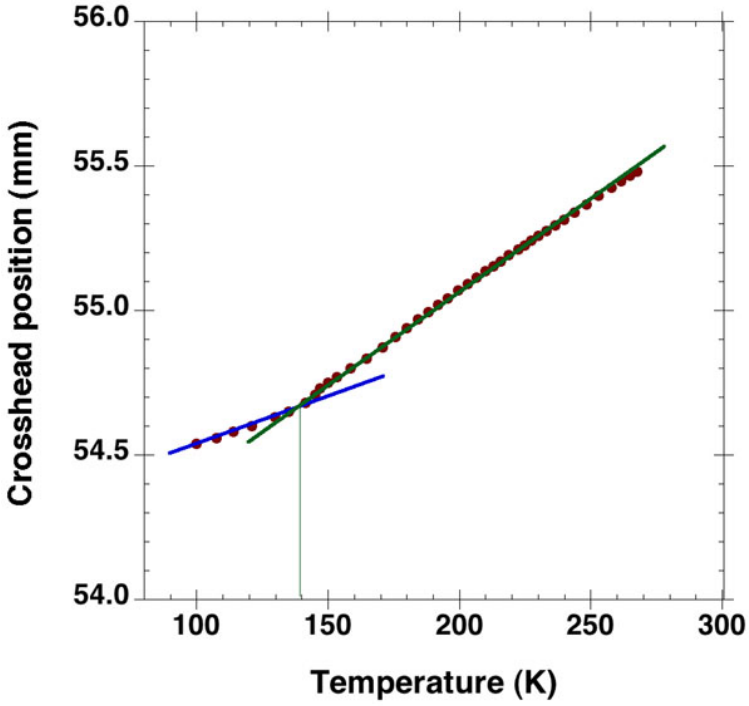

Figure 3.8 Cross-head movement vs. temperature during heat up (under load control) of compression sample compressed (to 2.5% strain) and unloaded at 95K.

3.4 Discussion

One of the notable features of this material is the tension-compression asymmetry. It can be speculated that the strain hardening in compression corresponds to a second deformation mechanism (such as slip) which is responsible for the smaller recovery than in tension. In tension, the plateau stress is extremely flat and all the strain is recovered. Also, the higher stress at the elastic limit in compression may correspond to a different deformation mechanism.

Corresponding to the recoverable and unrecoverable parts of the applied strains, distinct features were observed on the specimen surfaces. These experiments were done using the tensile rig of Figure 2.8.

Figure 3.9 shows polished faces of a tensile sample which was loaded to 10% strain and unloaded. Straight parallel lines appear on the surface in the pseudo-elastic region (Figure 3.9 (a)). The density of these lines increases as the applied strain is increased. These lines completely disappear when the sample was unloaded (Figure 3.9 (b)). Figure 3.9 (c) shows a diagram of the trace analysis done on these samples. The crystallographic planes (D_1 and D_2 in figure 3.9(c)) corresponding to the two faces (on the gage section) of a tensile sample are known (from Laue X-ray diffraction). These planes combined with the measured angles (θ_1 and θ_2) give the complete description of the planes formed by the traces on the two faces. This plane was found to be the (211) plane.

Tensile samples were loaded up to 13% strain which is beyond the fully recoverable strain limit and surface observations were made using SEM. Figure 3.10 (a) shows parallel lines (labeled Type1) corresponding to the pseudo-elastic region, which are the same as those in Figure 3.9 (a). As the sample is strained more than 10% a second type of wavy line (labeled Type 2 in figure 3.10 (b)) which look similar to slip lines, appear on the surface. These lines do not disappear on unloading the sample. Some of the Type 1 lines are also seen trapped between these Type 2 lines. Parts of the sample, where no Type 2 lines appear, become completely free of Type 1 lines on unloading. This is also consistent with the fact that only about 4% strain can be recovered from samples strained to 13%, whereas all the strain is recovered from samples strained to 10%. Therefore, some of the applied strain is trapped once plasticity sets in.

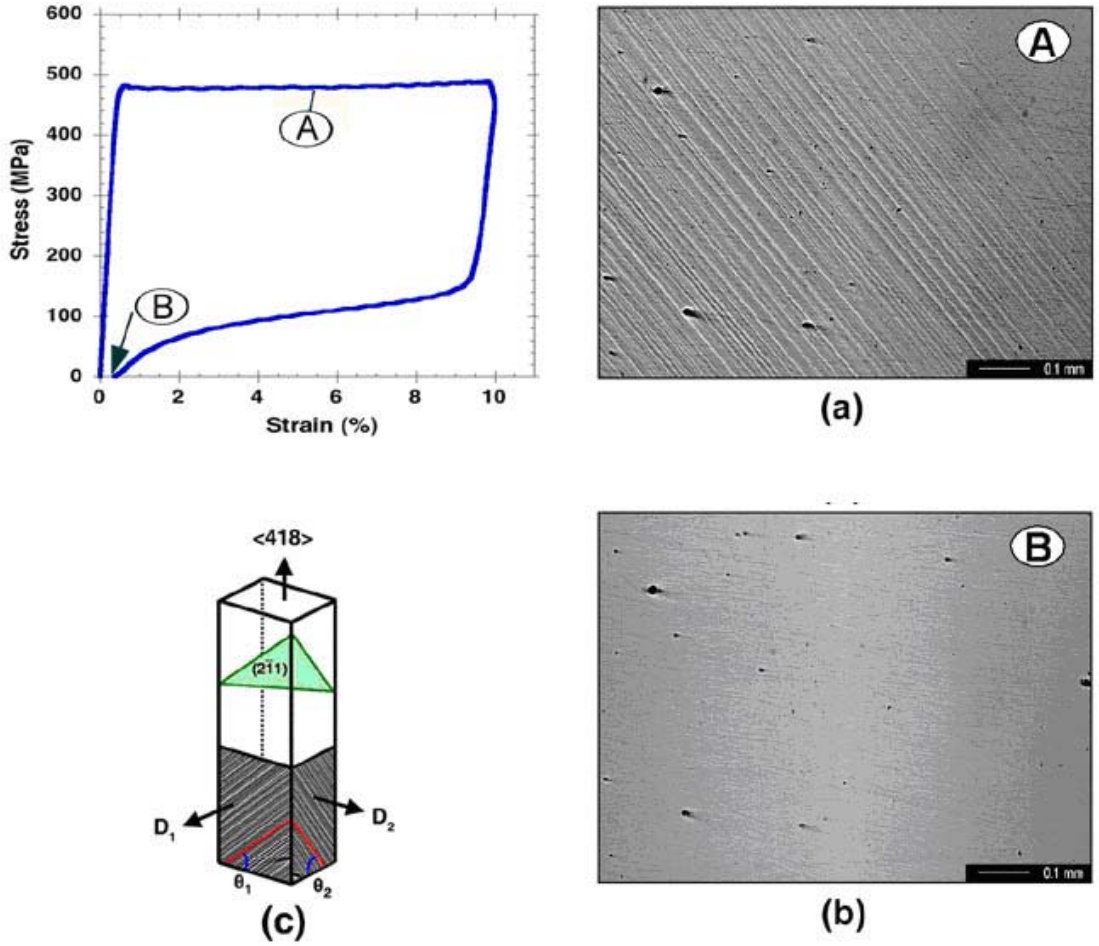

Figure 3.9 Optical micrographs showing (a) parallel lines (steps) that appear during pseudo-elastic deformation, and (b) the complete disappearance of these surface steps upon unloading.(c) Slip line trace analysis on two perpendicular sample surfaces (known orientations D_1 and D_2) shows that the parallel steps are traces of the (211) planes.

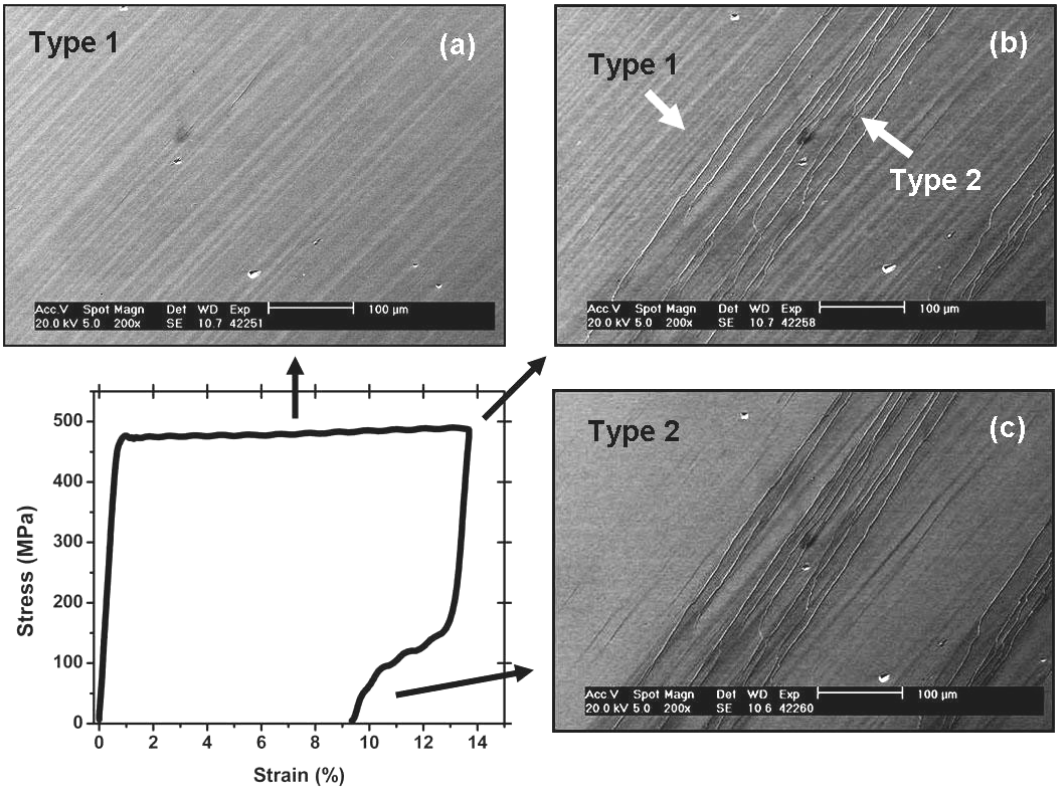

Figure 3.10 SEM micrographs showing (a) surface steps (Type 1 lines) in the pseudo-elastic region, (b) wavy slip lines (Type 2 lines) beyond ~ 10% applied strain, and (c) Type 2 lines remaining after unloading (many, but not all, of the Type 1 lines are gone).

Tensile stress-strain curves at various temperatures (Figures 3.5 and 3.7) show that there is no appreciable change in the plateau stress during loading in the temperature range -73°C to 100°C. However, the unloading plateau stress ($\boldsymbol{\sigma_r^T}$ in Figure 1.5) or the stress at which the maximum amount of recovery takes place increases constantly with increasing temperature. This behavior is typical of conventional SMAs [5], where the plateau stress increases linearly with temperature due to the Clausius-Clapeyron effect. In more general terms, this is indicative of a stress-induced transformation with some finite change in volume. The recovery stress, σ_r is plotted as a function of temperature in Figure 3.11. In each case, the initial elastic (linear) section and the flat plateau section of the unloading part were extrapolated to find σ_r at their intersection. A straight line fitted through the data points gives a slope of **526 kPa/K**. Assuming a single transformation, from the Clausius-Clapeyron equation we have:

$$\frac{d\sigma_r}{dT} = \frac{\Delta H_r}{\varepsilon T_r \Delta v} = 526 \text{ kJ/K-m}^3 \qquad (3\text{-}1)$$

Where ΔH_r is the enthalpy of reverse transformation, T_r is the transformation temperature, ε is the transformation strain and Δv is the volume change during the transformation. Unfortunately, since the values of T_r, ε and Δv are not known, the ΔH_r can not be found at this time.

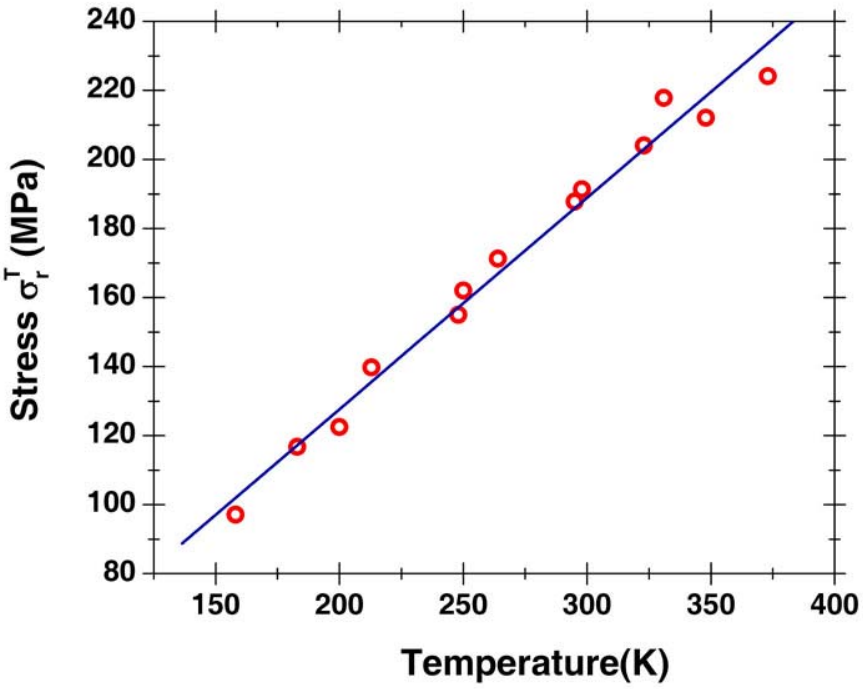

Figure 3.11 Unloading plateau stress σ_r as a function of test temperature. Straight line is fitted to obtain the slope of the curve.

The nature of stress-strain curves, appearance/disappearance of slip lines and the increase in the value of recovery stress with increasing temperature are very similar to traditional shape memory and pseudo-elastic materials. However, many other characteristics of these alloys are dissimilar to SMA's. Fe_3Al shows pseudo-elastic behavior only in single crystal form. It does not strain harden in tension, even at very high applied stresses. Shape memory effect was seen at very low temperatures unlike traditional SMA's which show shape memory effect at temperatures generally a few tens of degrees below 0^oC.

Chapter # 4

In Situ Neutron Diffraction Studies of Single Crystalline Fe_3Al

Deformation in materials with crystalline lattice occurs by dislocation motion, twins, phase transformations etc [78]. In order to distinguish these various deformation mechanisms the atomic arrangement needs to be observed during deformation. Diffraction techniques allow us to study the atomic arrangements in various crystalline materials by measuring the inter-planar distances between layers of atoms.

Neutron diffraction is discussed in this chapter with special emphasis on *in situ* deformation experiments and the time of flight technique. This is followed by results and analysis of *in situ* neutron diffraction experiments under uniaxial loads on single crystal Fe_3Al. A brief description of each of the neutron diffraction instruments used for the present study is given to explain the geometrical aspects of the experiments. The chapter concludes with a discussion of results.

4.1 Introduction to neutron diffraction

Diffraction has been used for almost a century to study the structure of crystalline materials [80]. The full mathematical description of diffraction can be found in several

books [9, 81] and will not be discussed here. It is however, important to mention Bragg's law [82]:

$$n\lambda = 2d \sin\theta \qquad (4\text{-}1)$$

which shows the relation between the d-spacing (d) of the crystallographic planes and the wavelength (λ) of the incident beam. The angle of the diffracted beam is θ and n is the multiplicity of the reflection. For the purpose of studying the crystal structure, d is the unknown quantity in many cases. This is one physical parameter of the crystal structure that we obtain from a diffraction pattern. Other physical quantities require a more rigorous mathematical description which will be developed as and when required in this chapter.

X-rays are the most widely used form of radiation for diffraction. The desktop X-ray diffractometers have various advantages like low production cost, relevant wavelengths, good intensity etc. One of the major disadvantages of this type of a system is that the depth of penetration of these X-rays in metallic samples is of the order of a few microns [9]. Therefore, we only get diffraction information from the near surface regions of the specimen. This problem of low penetration depth also persists with electrons [83].

Neutrons are the weapon of choice when high penetration depths are important. The wave nature of neutrons has been known for quite some time and the first diffraction

experiment was performed by von Halban in 1936 [84] . The fundamental laws of diffraction apply to neutrons in exactly the same way as X-rays. The difference lies in the fact that neutrons are not charged particles and have no electric field associated with them. Therefore, they are scattered by the nucleus of an atom as compared to the electron cloud in the case of X-rays and electrons. Since the scattering cross section of nuclei are orders of magnitude lower than that of the atoms, neutrons can penetrate much deeper. One of the direct consequences of this is that a much higher flux is required to get any significant diffraction.

Unlike X-rays and electrons which can be produced in desktop diffractometers and electron microscopes respectively, neutrons are harder to come by. Two of the most popular forms of neutron sources are reactor sources and spallation sources. Neutron sources are generally huge facilities with several instruments being fed by the same neutron source.

In reactor sources like HIFR at Oak Ridge National Laboratory and CNBC at Chalk River, neutrons are produced through a controlled nuclear reaction. The more preferred neutron sources these days are spallation sources at facilities like ISIS at Rutherford Appleton Laboratory , LANSCE at Los Alamos National Laboratory, IPNS at Argonne National Laboratory and SNS at Oak Ridge National Laboratory. In a spallation source neutrons are produced by bombarding a metal target with accelerated protons. A typical layout of a spallation source is shown in Figure 4.1 which shows the neutron diffractometers at the Lujan Centre at LANSCE. Note that the instruments are located in

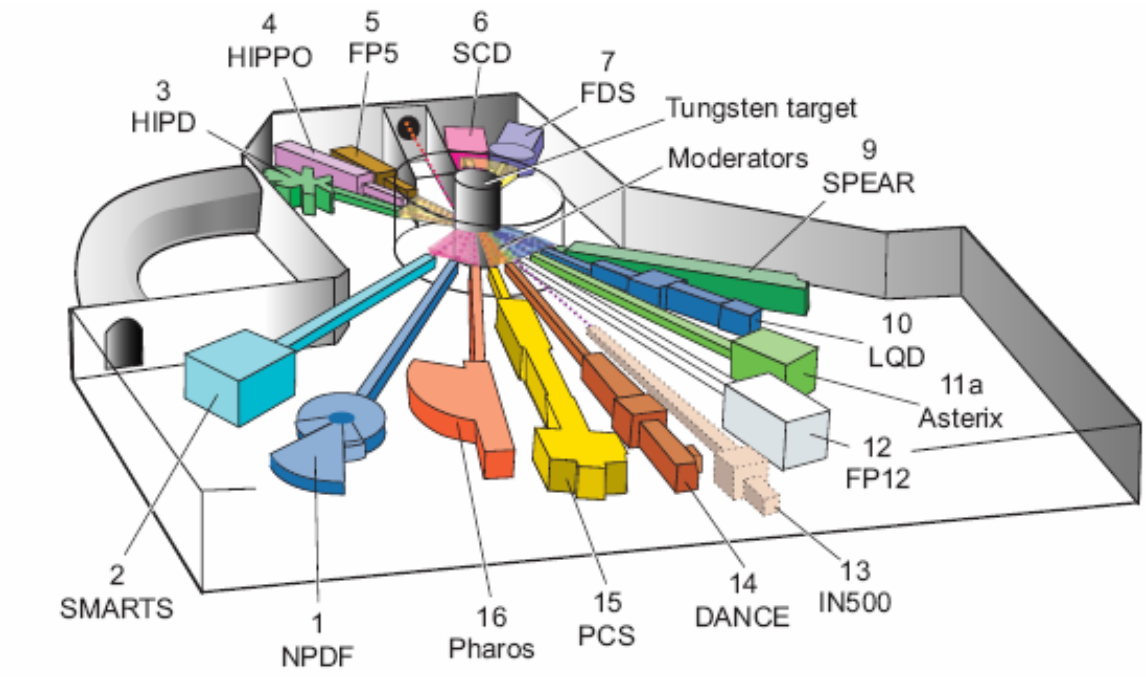

Figure 4.1 Layout of neutron diffractometers at the Lujan Centre at LANSCE.

a circle around the source. This is because the absence of charge on the neutrons make it extremely difficult to bend their path. Spallation sources allow the time of flight (TOF) measurement technique to be applied to diffraction experiments which provides an added level of flexibility in data analysis. TOF is discussed in detail in a later section.

4.1.1 *In situ* neutron diffraction with deformation

The high penetration depth of neutrons and their non-destructive nature allows immense flexibility in designing experiments. The use of bulk samples makes it easier to manipulate the sample as well as the sample environment during the diffraction. Therefore *in situ* experiments can be designed where neutron diffraction is performed while applying load, pressure, magnetic fields etc. to the sample. Also the sample can be kept at various temperatures, gas environments, vacuum etc.

This flexibility in designing experiments has attracted the interest of scientists who study the mechanical behavior of crystalline materials. The desire to learn various changes in the crystal structure (*d*-spacings of various planes, texture, phase transformation, twinning etc.) during deformation prompted the interest in the design of *in situ* deformation neutron diffraction experiments. Recently, a number of neutron diffraction instruments optimized for such measurement (e.g. NPD and SMARTS at LANSCE, ENGIN and ENGIN X at ISIS) have been built. A more comprehensive review of in situ experiments can be found in reference [85]. The basic idea behind these instruments is to simultaneously study the transversely and longitudinally oriented planes

of the crystal during uniaxial loading. This is achieved by having an instrument geometry which uses two detectors at 45^{o} to the loading axis as shown in Figure 4.2.

The diffraction measurements are done at various stress/strain levels as the sample is loaded. However, depending on the neutron flux and the material being studied, each measurement can take a few minutes to obtain a decent diffraction pattern. Therefore all parameters like load, strain, temperature etc. have to remain stable during the measurements. Although these experiments are not truly real-time due to the above reason, the ability to get a full diffraction pattern without moving the load rig greatly increases the accuracy of the data. Also, in cases like pseudoelastic materials, where unloading has a reverse affect on the crystal structure *in situ* experiments are the only way to study the effect of straining on the crystal structure.

4.1.2 Time of flight (TOF) technique

The time of flight technique is a unique technique used to measure the neutron diffraction patterns. This is not a full review of the TOF technique but only the aspects relevant to the present experiments are discussed. TOF is the preferred measurement technique for pulsed neutron sources. These types of measurement are routine nowadays because of the greatly increased accuracy and speed of modern data acquisition systems.

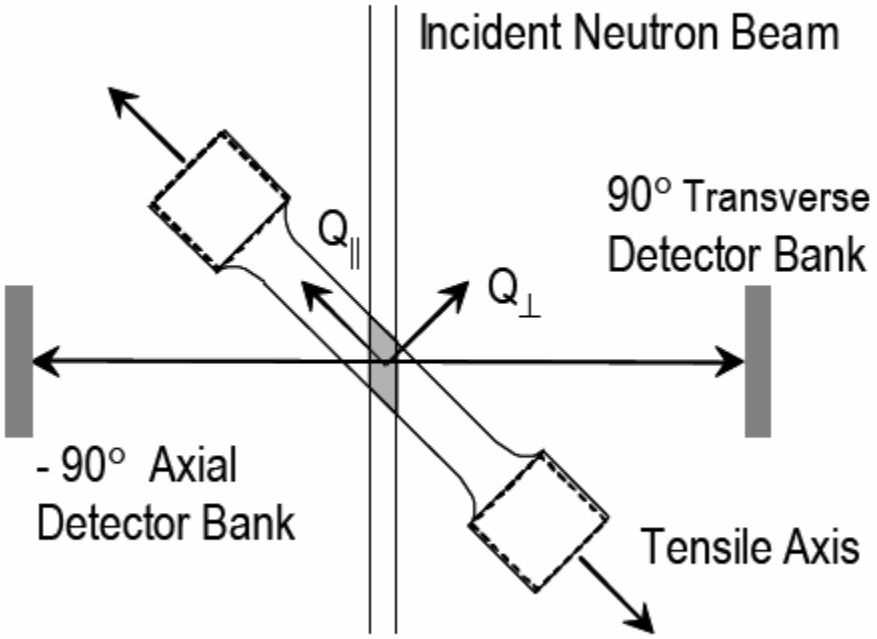

Figure 4.2 Geometry of a typical *in situ* neutron diffraction instrument.

TOF can be explained using the schematic in Figure 4.3, which shows a neutron source in relation to a neutron diffractometer. The red pulse which represents a proton pulse hits the target at regular intervals. Let us consider one such pulse which hits the target at t = 0. This produces neutrons with a whole spectrum of energies which take off radially from the target or the neutron source. Some of these neutrons are channeled to the sample (green beam) which is sitting in a diffractometer at a distance L_1 from the source. The neutrons from one pulse, which start off together, are now separated because they have different energies (and thus velocities).

When a neutron finds the right plane with d-spacing corresponding to its energy (according to Bragg's law) then it is diffracted. Let us say one such neutron's path corresponds to the blue path in the schematic. The detectors of neutron instruments (which have been used in the present study) are comprised of various tubes, the positions of which are accurately known. When a neutron hits a particular tube the event is recorded by the data acquisition system and the exact time of the event is noted. Let us say that this particular neutron happens to hit the detector at $t = t_1$. Since the lengths of the source to the sample (L_1) and from the sample to the tube (L_2) are known the total path traveled by the neutron is known. Therefore the velocity of this neutron can be calculated. This velocity then translates into the wavelength (λ) of the diffracted neutron through the well known wave-particle duality equation. The wavelength (λ) and the diffraction angle (θ) for the tube can be plugged into the Bragg's Law (equation 4-1) to calculate the d-spacing corresponding to this neutron. By summing over all the tubes (a process called binning) a full intensity vs d-spacing pattern can be obtained.

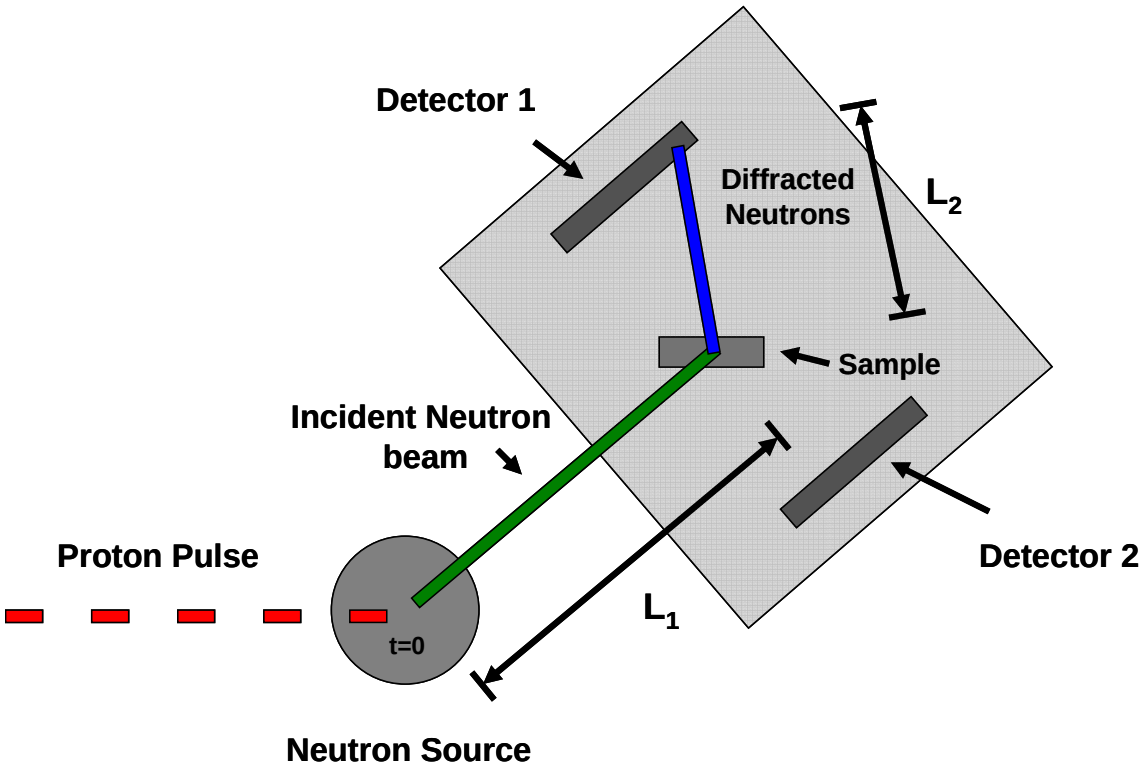

Figure 4.3 Time of Flight measurements at a pulsed neutron source.

In practice, the calculations described above remain hidden under instrument parameters and huge polynomial equations. The instruments are calibrated from time to time and the parameters that these calibrations yield, take care of the above calculation. Also in the analysis above, it has been assumed that successive pulses of neutrons are well separated so that the neutrons from one pulse do not interfere with the neutrons of the next. This may not be true for all instruments and sources. There exist other techniques, like a chopper, whose timing is coordinated with pulse timing, in the path of the neutrons so as to chop off a part of the neutron spectrum. However, for a fundamental understanding of the TOF technique the above simple analysis is enough.

4.2 Experimental results

4.2.1 SMARTS diffractometer

The SMARTS (Spectrometer for Materials Research at Temperature and Stress) diffractometer at the Los Alamos Neutron Science Centre (LANSCE) facility of the Los Alamos National Laboratory (LANL) is a 3rd generation neutron diffractometer. It is optimized for polycrystalline materials with *in situ* loading and temperature capabilities. Figure 4.4 shows a schematic of the diffractometer and Figure 4.5 shows an inside view of the diffractometer.

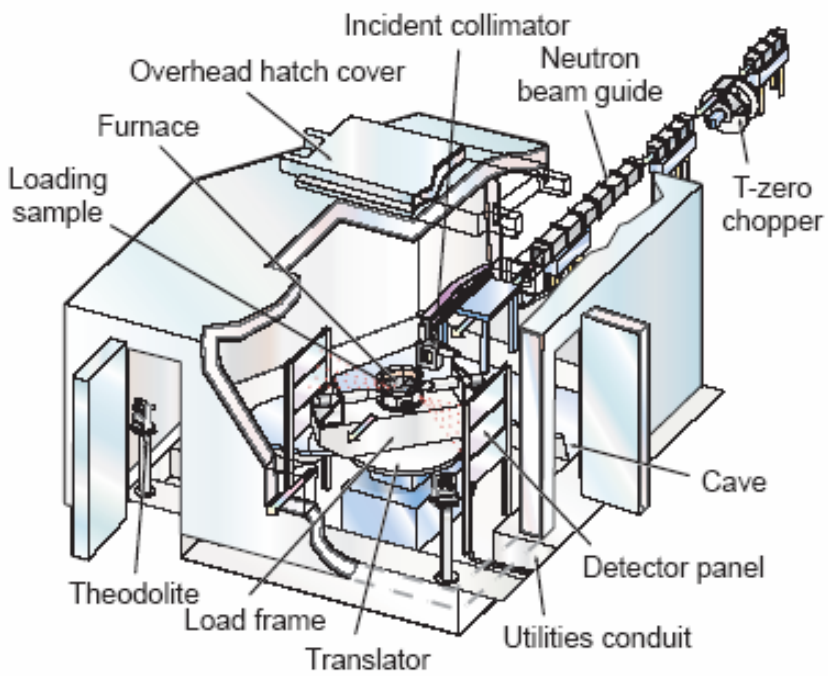

Figure 4.4 Schematic of the SMARTS diffractometer at LANSCE.

Figure 4.5 Inside view of the SMARTS diffractometer at LANSCE. The load frame can be seen in the centre of the image and the transverse detector bank is on the left.

The diffraction geometry is the same as shown in Figure 4.2. A 250 kN Instron® load frame sits at 45° to the incident beam in the middle of the cave. There are two detector banks on either side of the incident beam. The whole setup sits on a circular stage which can be programmed to rotate/oscillate. The high temperature furnace mounts on top of the load frame. The furnace can be replaced by a cryogenic setup which is capable of temperatures as low as 90 K. The instrument is about 32 meters from the neutron source which gives the neutrons of different energies enough time to spread out sufficiently in space so as to provide good d-space resolution.

4.2.2 Room temperature compression in SMARTS

SMARTS is a diffractometer which is optimized for measurements on polycrystalline samples. A polycrystalline material, assuming no texture and a large number of grains, has a random distribution of grains which are oriented in all possible orientations. Therefore, a large number of neutrons of any energy will find a favorably oriented grain and diffract. This principle is illustrated in the schematic of Figure 4.6. Each of the incident neutrons of different energy finds a plane where Bragg's law is satisfied. Ideally, the amount of diffraction would be uniform around the sample. Therefore each detector tube will be able to see peaks corresponding to each allowable reflection of the crystal. This gives a full diffraction pattern of the polycrystalline material.

The case of a single crystal is shown in Figure 4.7. In this case only neutrons

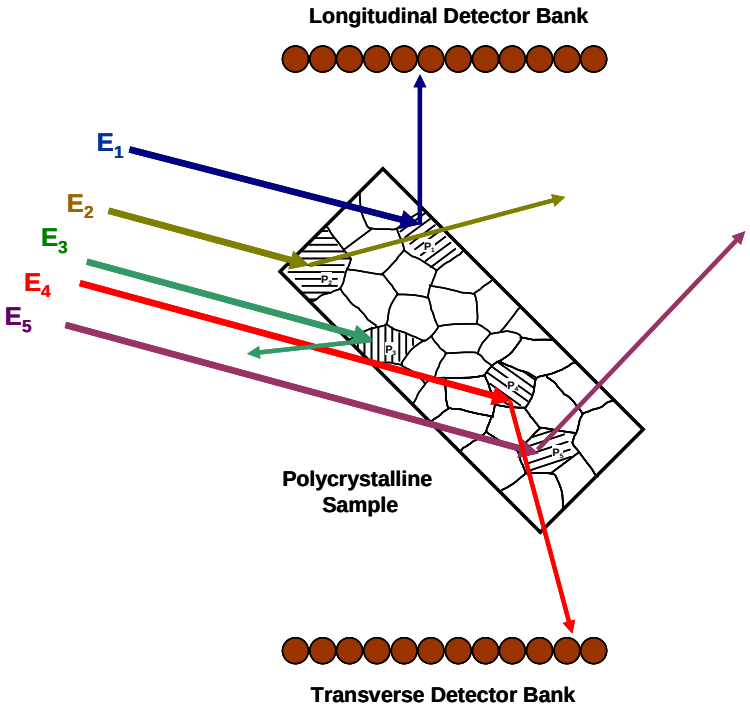

Figure 4.6 Schematic showing the diffraction of neutrons by a polycrystalline sample.

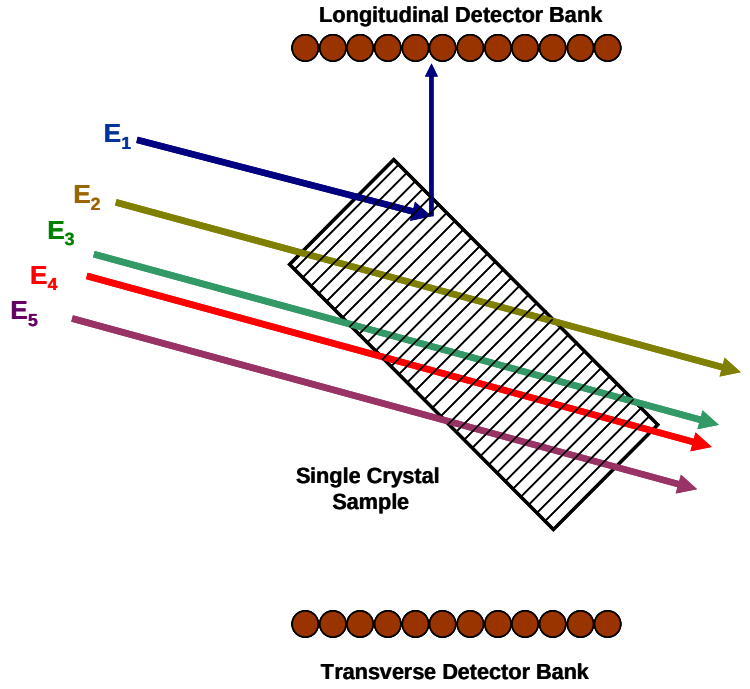

Figure 4.7 Schematic showing the diffraction of neutrons by a single crystal sample.

with energy E_1 find favorably oriented planes and diffract. The other energies do not find any plane which satisfies Bragg's law and are either absorbed or simply transmitted. The net result is that all planes of the single crystal will diffract their respective neutrons with the right energies but since these planes are oriented in specific directions with respect to the detector position, the detectors, with their fixed coverage can only see a limited number of these planes.

Single crystal Fe_3Al samples were compressed in the <418> crystallographic direction. As discussed in chapter one, this direction was used because along this direction, maximum amount of strain is recovered during uniaxial tests. The compression samples were cylindrical with a diameter of 6 mm and length of 14.4 mm. These were loaded on the SMARTS load frame and compressed. The stress vs crosshead displacement curve is shown in Figure 4.8 (a). Since a direct strain measurement was not used due to limitations of sample size, the crosshead displacement was used as a representation of strain. Fortunately in the non-elastic region (pseudoelastic/plastic), the stress increases only by a small amount and therefore most of the deformation is taking place in the sample. This means that the compliance of the machine represents a very small portion of the strain in this region. Due to the above reason the crosshead displacement in a very close representation of the strain in the non linear region. Neutron diffraction patterns were taken at different points along this loading curve. The dips in the curve represent points at which the loading/straining was stopped and a neutron diffraction pattern was recorded.

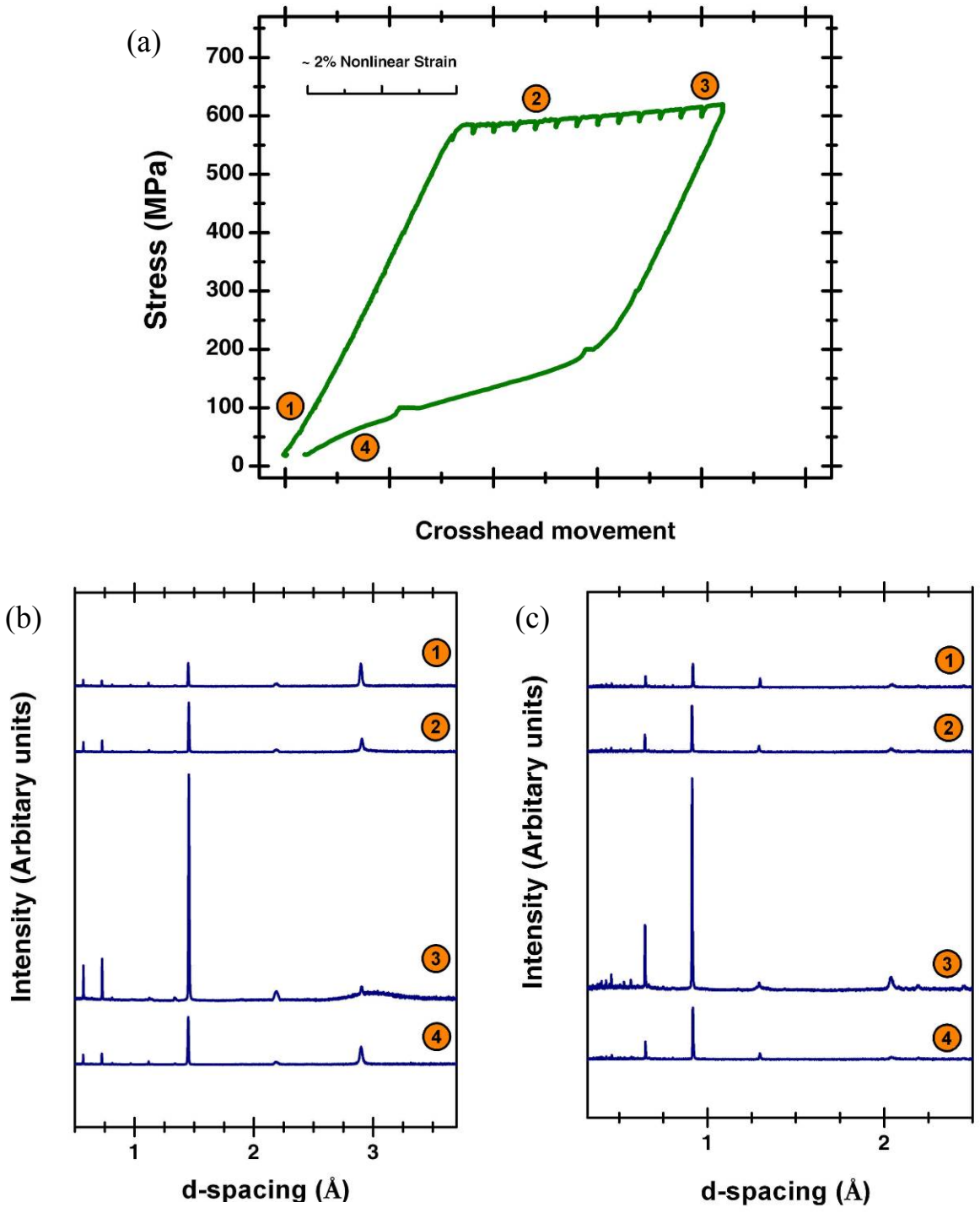

Figure 4.8 Evolution of diffraction pattern along one stress-strain curve cycle. (a) Stress vs Crosshead displacement showing points 1 through 4 where the above diffraction patterns were recorded by the (b) transverse bank (c) longitudinal bank.

Figure 4.8 (b) and (c) show four representative diffraction patterns taken at different points on the loading curve from transverse and longitudinal banks respectively. The first obvious result is that, the intensities of various peaks change as the sample is loaded in the non linear region. Some peaks change by as much as 3 times their original intensities. These intensities go back, close to their original values as the sample is unloaded to zero load.

The diffraction patterns of Figure 4.8 have been indexed and shown in greater detail in Figure 4.9. The bottom plots in each of the series of diffraction patterns represent zero strain and the ones above are in order of increasing strain, the top one being at maximum strain. The diffraction pattern in the unloaded condition is not shown in these plots. The indexing of the peaks was done on the basis of the DO_3 structure shown in Figure 1.11. The fundamental peaks are labeled in red while the superlattice reflections are labeled in green. This convention is followed throughout the rest of the text. The blue ticks at the base of the plots are the positions of the $D0_3$ reflections.

As was expected for a single crystal the entire diffraction pattern including all allowable reflections is not captured by the SMARTS detectors. In the longitudinal bank we expect reflections which are close to the axial direction, which is the <418> crystallographic direction in this case. Therefore we see reflections like 420 and 620 which are only a few degrees away from the <418> direction. The transverse bank is expected to show a portion of the band of reflections perpendicular to the <418> direction. In this case, one of the most significant set of reflections is the 200 series which is almost perpendicular to <418>.

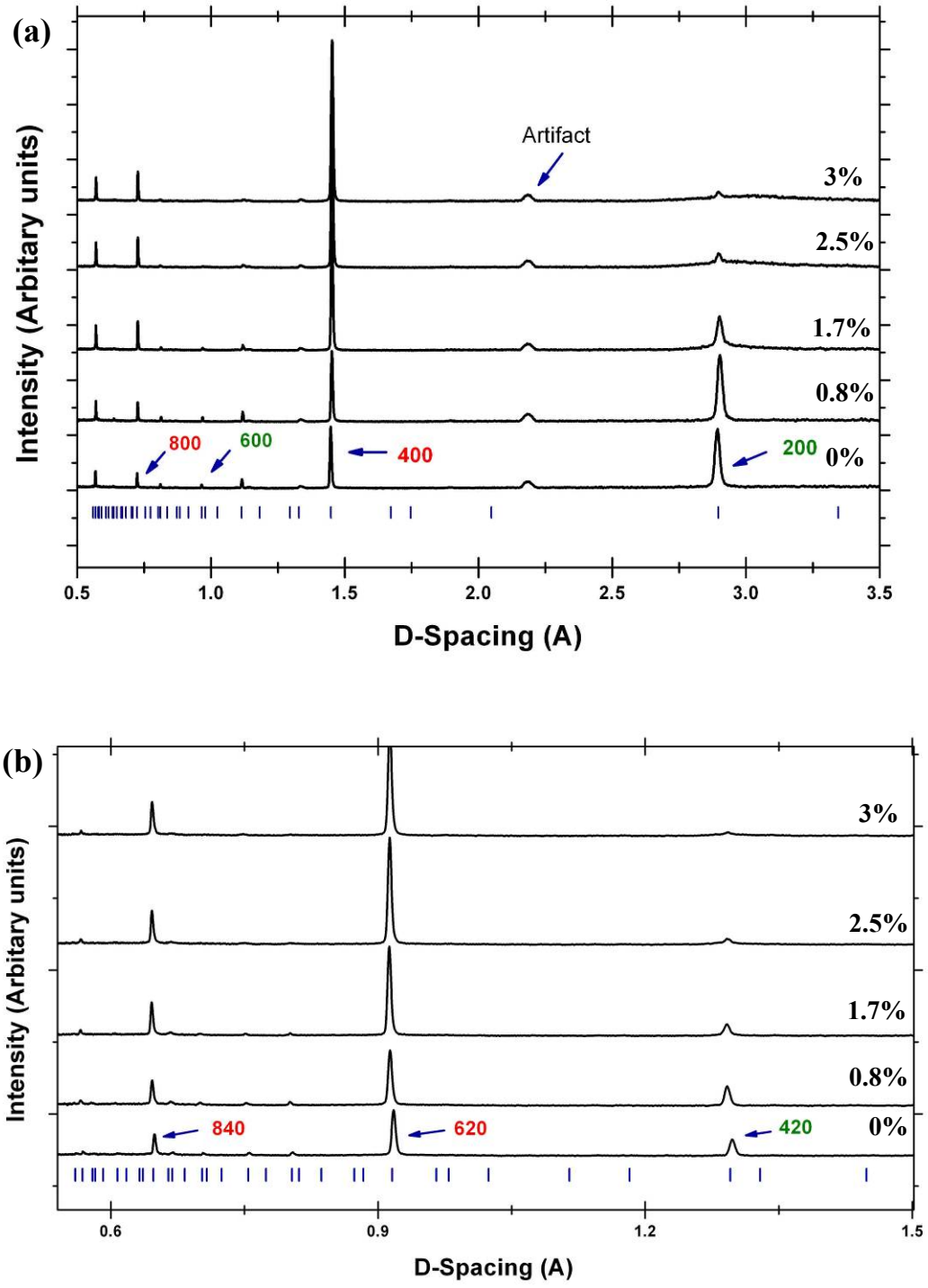

Figure 4.9 Indexed diffraction patterns of sample compressed in the <418> crystallographic direction from (a) transverse bank and (b) longitudinal bank. Bottom plot is at zero strain and the strain increases progressively in each of the upper plots.

One of the distinct features of these plots is that most of the fundamental peaks become stronger while the superlattice peaks lose intensity. Some of the finer features of the diffraction pattern which cannot be clearly distinguished from these plots are discussed in a later section.

4.2.3 Strain dependence of peak intensities

Changes in peak intensities are closely related to the pseudoelastic strain on the sample. Figure 4.10 (a) shows that the peak intensities of the 422 peak from a similar experiment in the SMARTS diffractometer along with the stress-strain curve where only the pseudoelastic part of the strain has been plotted. The peak intensities were normalized such that the maximum peak intensity equals the maximum strain. The peak intensities follow the stress-strain curve very closely. Figure 4.10 (b) shows the intensities plotted as a function of the pseudoelastic strain. The intensities vary linearly with the strain.

4.2.4 Compression in other orientations

As discussed above, the SMARTS diffractometer has limited detector coverage in space and is ideally suited for polycrystalline samples. Only a handful of peaks could be captured in the diffraction pattern from a single crystal. Additional limitation was imposed because the pseudoelastic property is maximized in certain crystallographic direction, which then fixes one of the axes of our crystal namely the <418> direction.

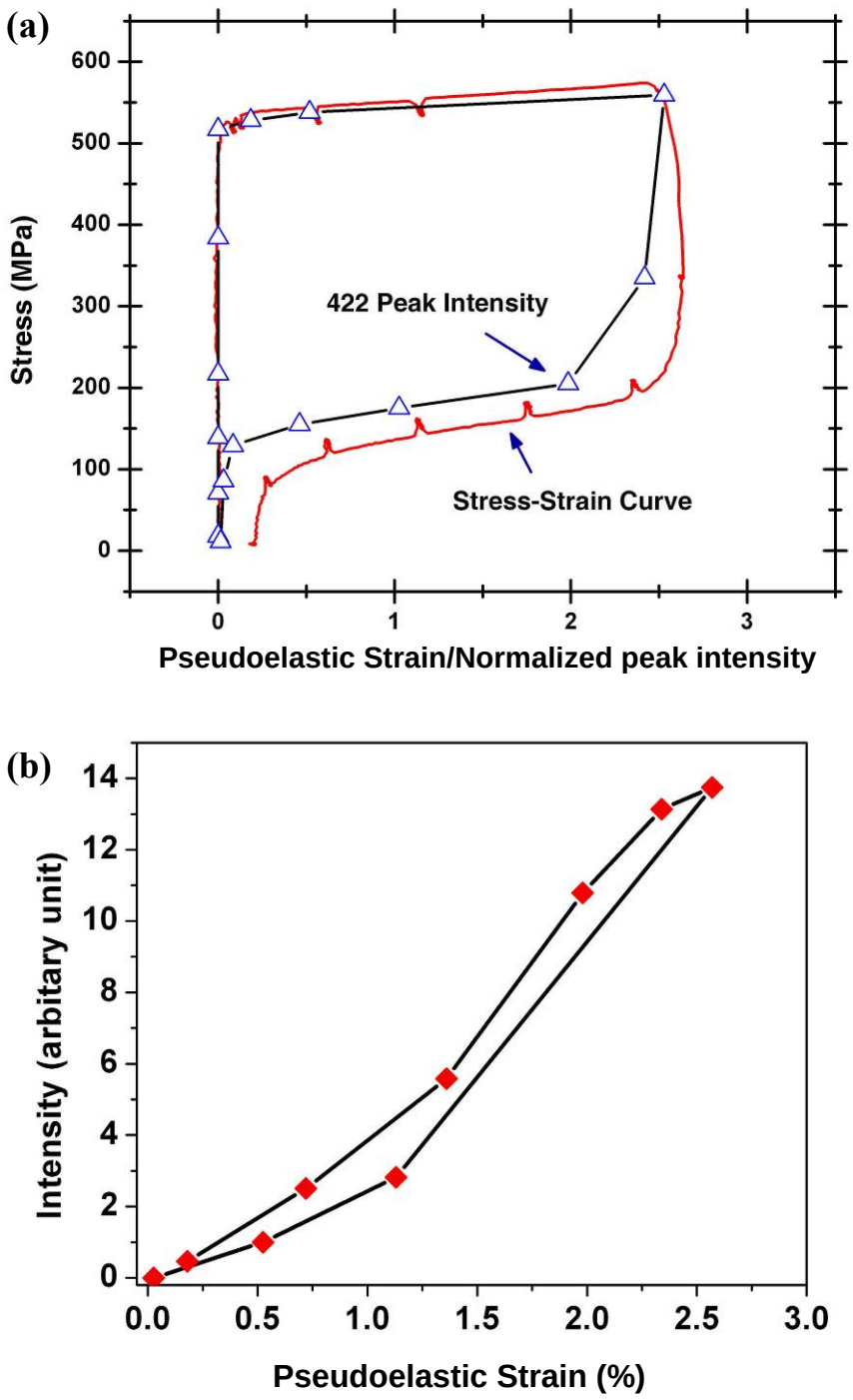

Figure 4.10 (a) Pseudoelastic part of the stress-strain curve plotted with the peak intensity of the 422 peak as a function of stress. (b) peak intensity as a function of strain.

This meant that the peaks falling in the longitudinal bank would be expected to be identical and these are the peaks near the 418 (compressive direction) reflection in a stereographic projection. The reflections which fall in the transverse bank have a wider range and will depend on the rotation of the sample about the compressive axis. Nevertheless, these are also a limited number of reflections depending on the compressive direction.

Although a full diffraction pattern can not be obtained, it might be possible to capture some of the important low index peaks by slightly changing the loading direction. As shown by Yasuda et. al. [73] single crystals show significant amounts of strain recovery close to orientations like 145 and 144.

Therefore, the next set of experiments involved compression of single crystal with orientations 144 and 145 in the SMARTS diffractometer. These samples were cuboids in shape with dimensions 6 mm x 6 mm x 14.4 mm. The cuboidal shape facilitated the positioning of the samples in the correct orientation on the diffractometer such that one of the low index reflections was detected by the transverse detectors.

Figures 4.11 and 4.12 show the resulting diffraction pattern evolution. The samples were compressed to ~3% total strain in each case almost all of which was recovered owing to the pseudoelastic nature of the material. The bottom plots represent zero strain and the top plot represents maximum strain. The 111 and 110 families of reflections are seen in the transverse bank of the sample compressed in the 145 and 144 directions respectively. Trends similar to the 418 sample are seen in these two cases where the fundamental peaks increase in intensity and the superlattice peaks decrease.

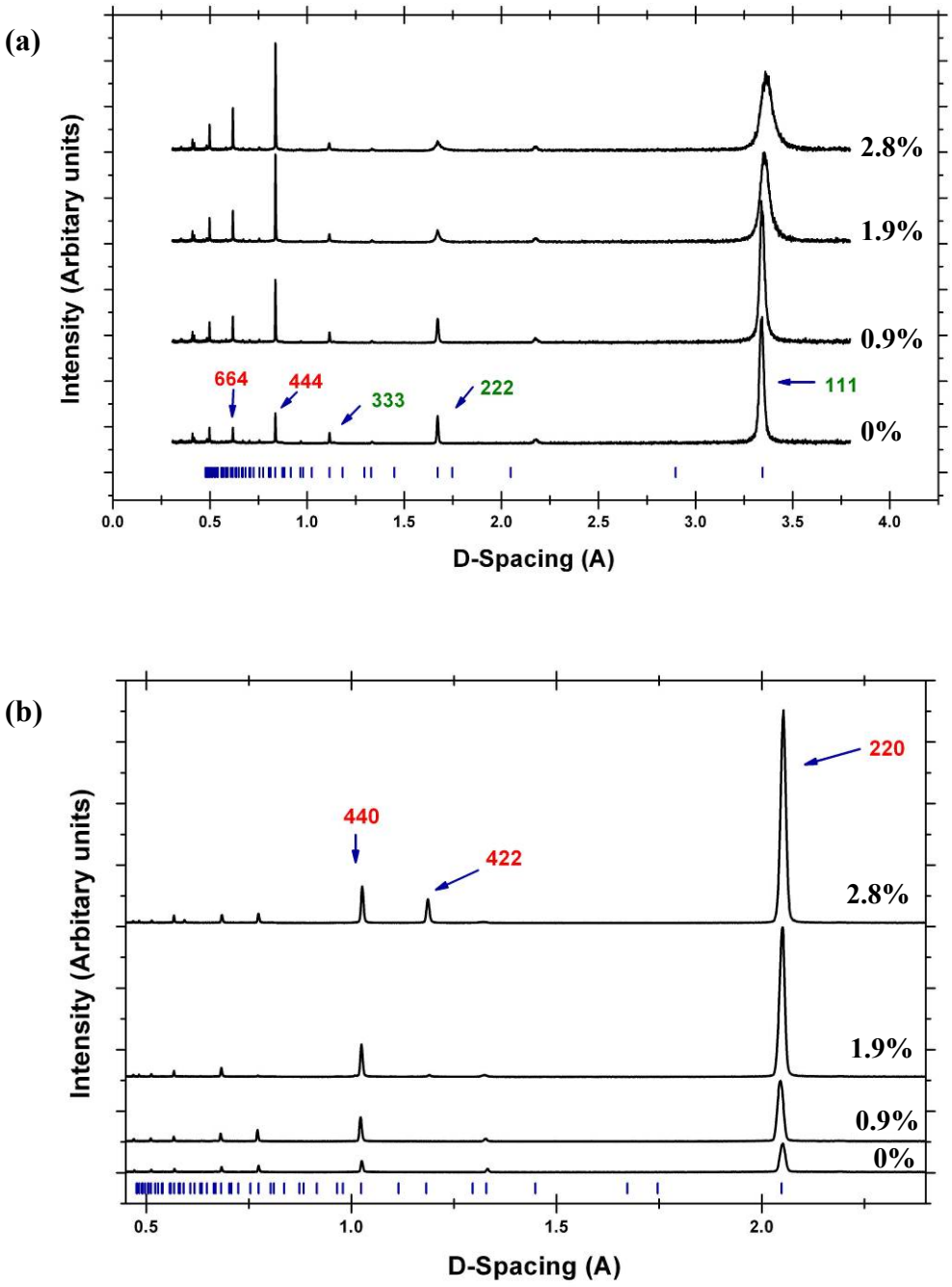

Figure 4.11 Indexed diffraction patterns of sample compressed in the <145> crystallographic direction from (a) transverse bank and (b) longitudinal bank. Bottom plot is at zero strain and the strain increases progressively in each of the upper plots.

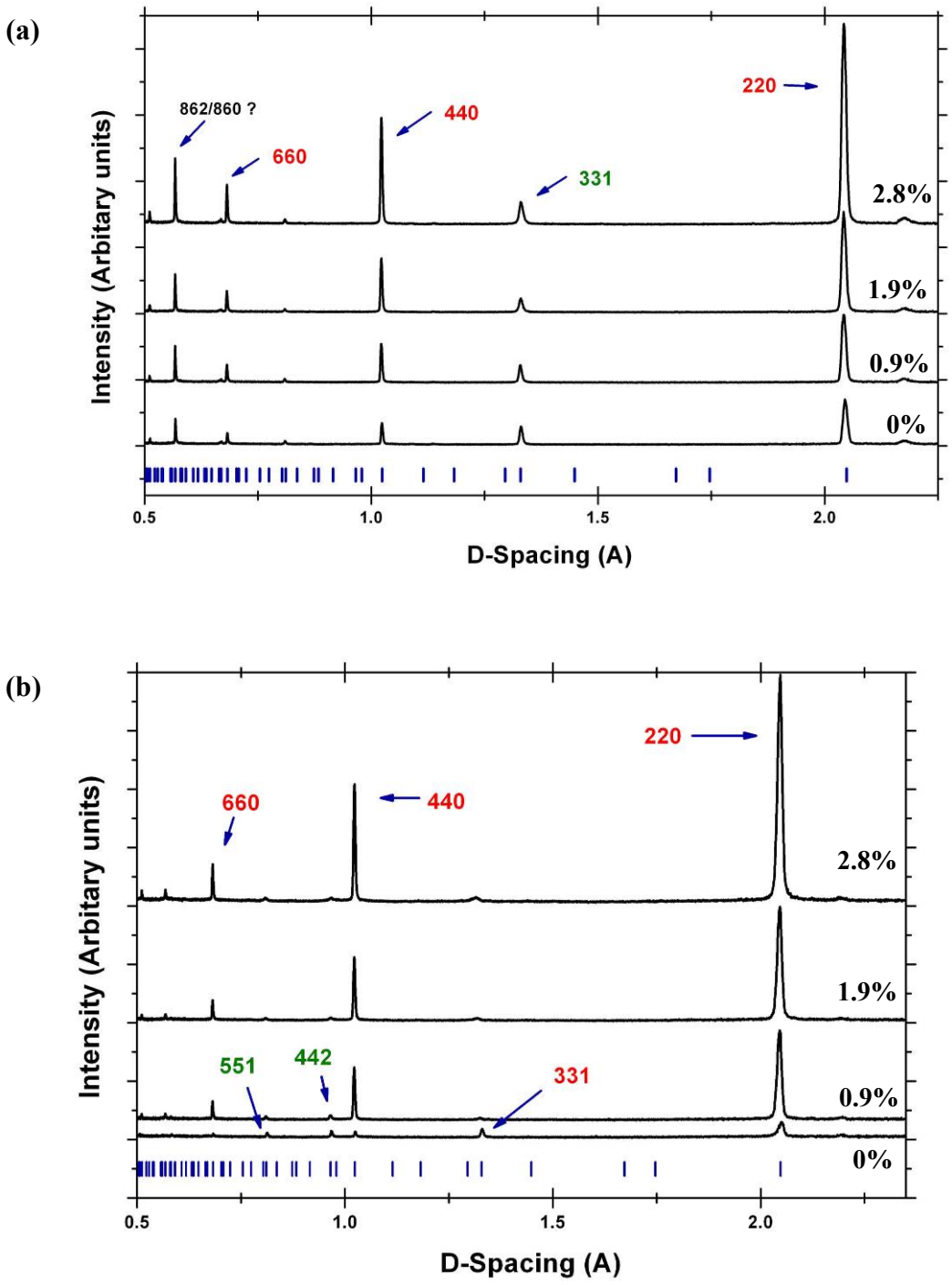

Figure 4.12 Indexed diffraction patterns of sample compressed in the <144> crystallographic direction from (a) transverse bank and (b) longitudinal bank. Bottom plot is at zero strain and the strain increases progressively in each of the upper plots.

4.2.5 Individual peak behavior

Peaks from the above diffraction pattern were fitted individually and parameters such as d-spacing, intensity, peak breadth etc. were obtained. Figure 4.13 shows peak intensity and micro strain as a function of the crosshead movement for the 100 and 111 type peaks. The two peaks are from two different experiments on different samples. The peak intensities have been normalized such that the intial peak intensity in each case is one. Micro strains are defined as

$$\varepsilon_{\mu} = \left(\frac{d_{hkl}}{d^{0}_{hkl}} - 1\right) \times 10^{6} \qquad (4\text{-}2)$$

where d_{hkl} is the d-spacing of the hkl reflection and d^0_{hkl} is the initial d-spacing. Microstrains are used as a representation of the normalized peak position to compare the relative movements of the peaks.

As seen from the plots, the different peaks of the same family (100 or 111) behave differently. The peak intensities do not change significantly in the elastic region as was expected but change by a huge amount as the pseudoelastic strain increases. The intensities of all the fundamental reflections increase while those of the superlattice decrease. The intensities of the 400, 800 and 444 increase by about 300-400 % while the decrease in the intensity of 600, 111, 222 and 333 is about 20-50%. The 200 peak almost entirely vanishes. The microstrains of 200/600 and 400/800 pairs seem to move together but microstrains of the 111 family changes independent of each other.

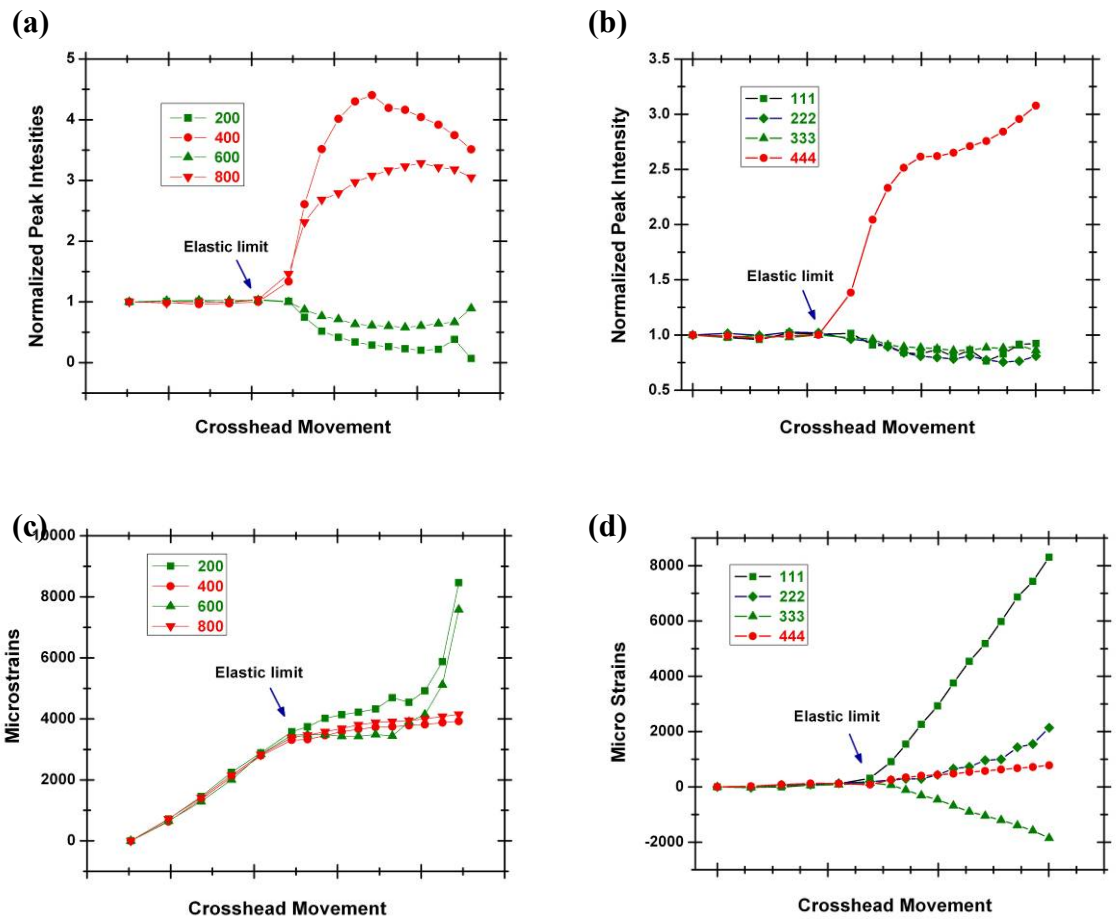

Figure 4.13 (a) and (b) show how the peak intensities of the 100 and the 111 family of reflections vary in the transverse bank as a function of strain. (c) and (d) show the micro strains of the same reflections.

4.2.6 New peaks

A closer inspection of the diffraction pattern yields the appearance of certain new peaks upon the application of strain, the most distinct of which are presented here. The first of these peaks can be seen from the diffraction pattern of Figure 4.9 (a). This peak appears as a broad peak near the disappearing 200 peak. When plotted on an expanded vertical scale it can be distinctly seen as shown in Figure 4.14. Figure 4.14 (a) is the diffraction pattern before straining the sample. Figure 4.14 (a) and (b) are on the same scales for comparison. The new peak can clearly be seen at a d-spacing which is slightly higher than the 200 d-spacing. This new peak disappears as we unload the sample.

Figure 4.15 is a series of plots of the raw neutron diffraction data obtained from the ISAW software. The vertical scale represents the tube number of the detectors of the neutron instrument. The horizontal scale is the d-spacing. The brightness of the spot (in this case the darkness) is a measure of its intensity. The way in which the tubes are numbered caused the pattern to break into two parts as in Figure 4.15 (b) and (c) with a blank band in between. As the sample is strained, 4.15 (b) and (c), the intensity of the 200 peak decreases. At the same time the new peak discussed above (Figure 4.14) appears as a streak and becomes more intense with further straining. Upon unloading the new peak disappears.

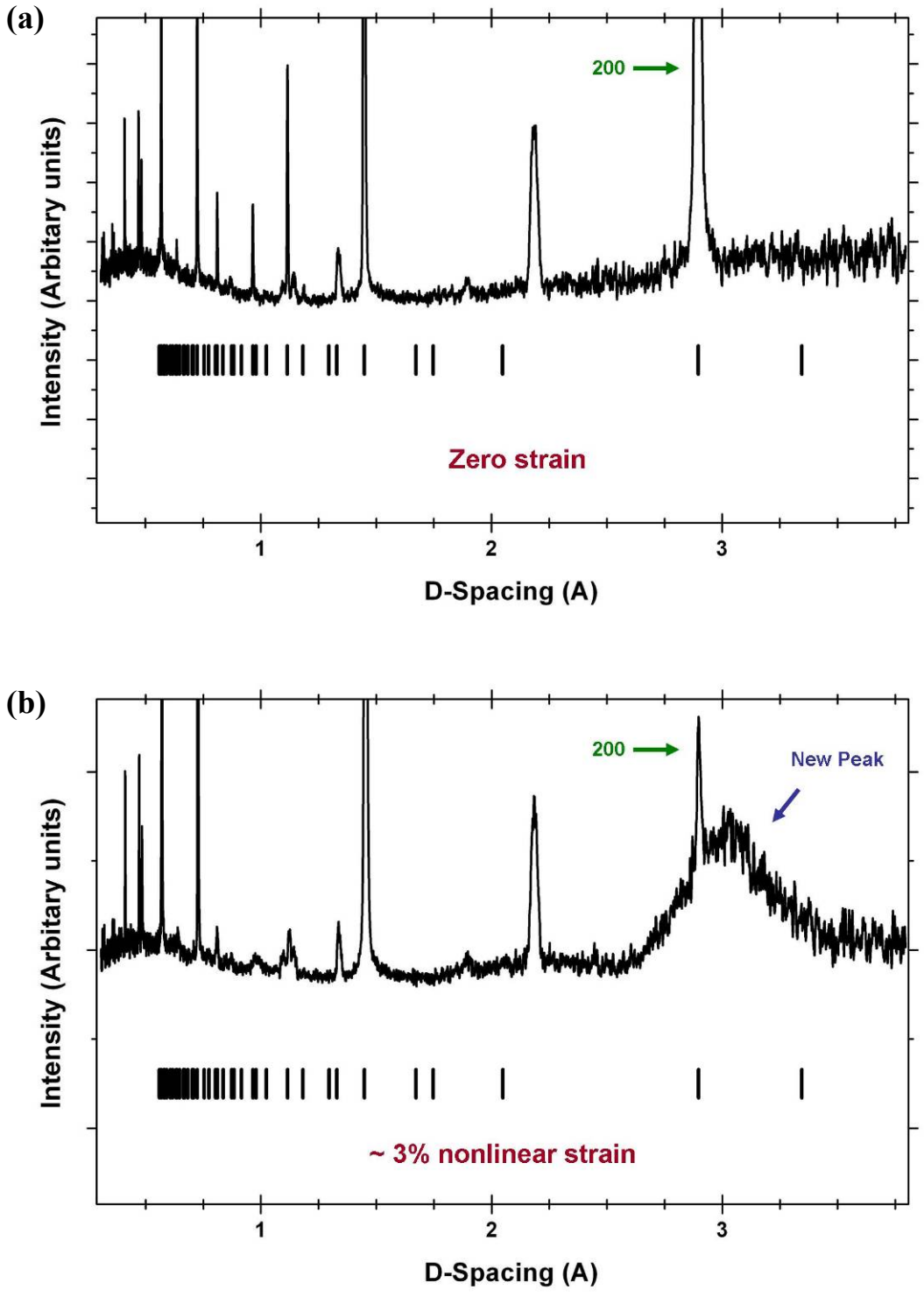

Figure 4.14 The transverse bank diffraction pattern showing a new peak in (b) near the original (a) 200 reflection

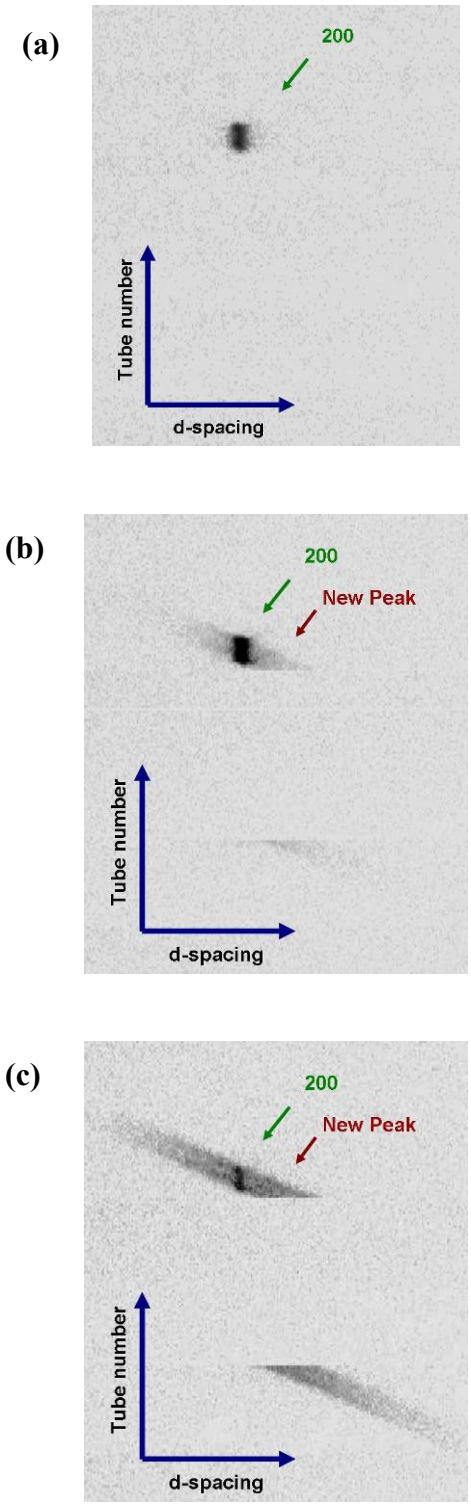

Figure 4.15 Laue-like images (ISAW images) drawn from the raw diffraction data showing the new peak. (a) zero strain (b) ~2% strain (c) ~3% strain

A separate new peak with a character quite different from that described above is seen near the 400 reflection. It appears as a small satellite reflection near the 400 peak (Figure 4.16). The peak intensity is quite small and is not detected in the binned diffraction pattern as it is lost in the background. However if the data are plotted one tube at a time, the new satellite reflection appears in the same tubes as part of the 400 peaks. Data from five such tubes have been plotted in Figure 4.16. The peak disappears upon unloading the sample.

4.3 HIPPO instrument

HIPPO (High-pressure preferred orientation neutron diffractometer) is a 3rd generation neutron diffractometer at LANSCE. The short beam path (~ 9 m) allows high neutron flux and thus good intensities although at the cost of some resolution in d-space. The most unique feature of HIPPO is its huge detector coverage. The instrument has five sets of detectors from 10^{o} to 150^{o} scattering angles, as shown in Figure 4.17 (a). Figure 4.17 (b) and (c) compare the detector coverage of the SMARTS and the HIPPO instruments in angular space shown on a stereographic projection.

Although primarily used for the measurement of preferred orientations and for high pressure experiments the diffractometer has diverse capabilities. The design of the instrument allows different modules to be lowered into the diffractometer. Among the various modules that were available the CRATES module was of interest in the study of

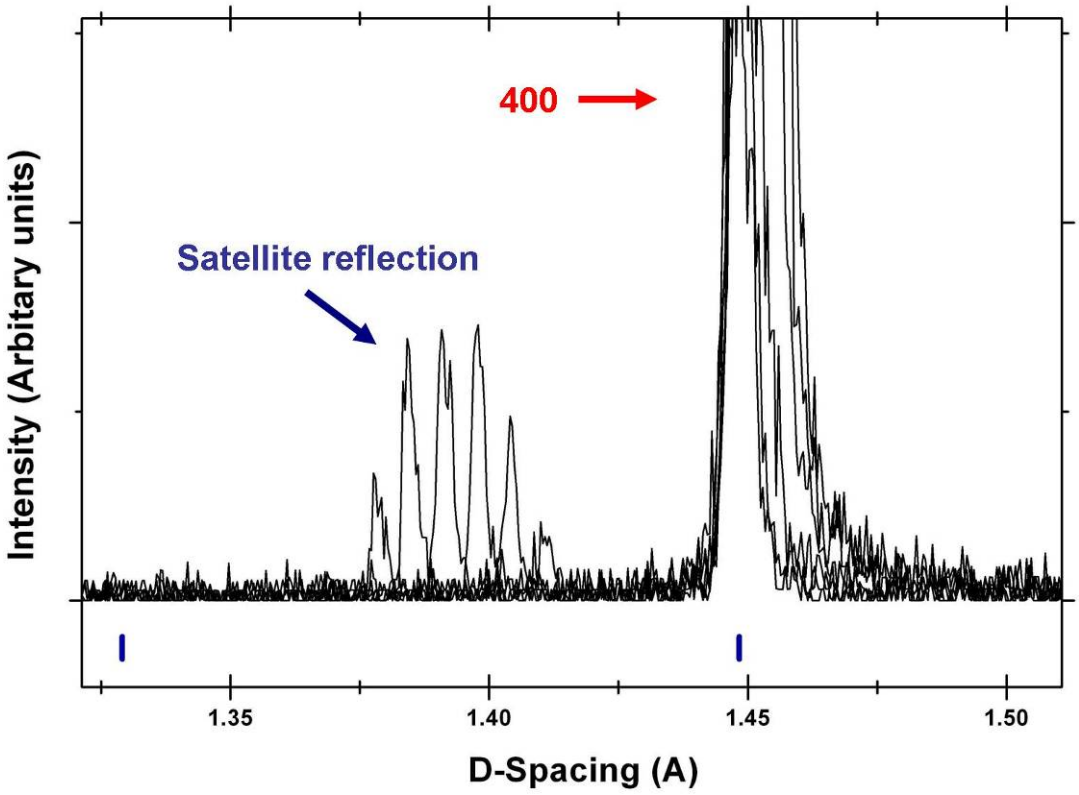

Figure 4.16 Satellite reflections seen near the 400 peaks upon plotting the data one tube at a time.

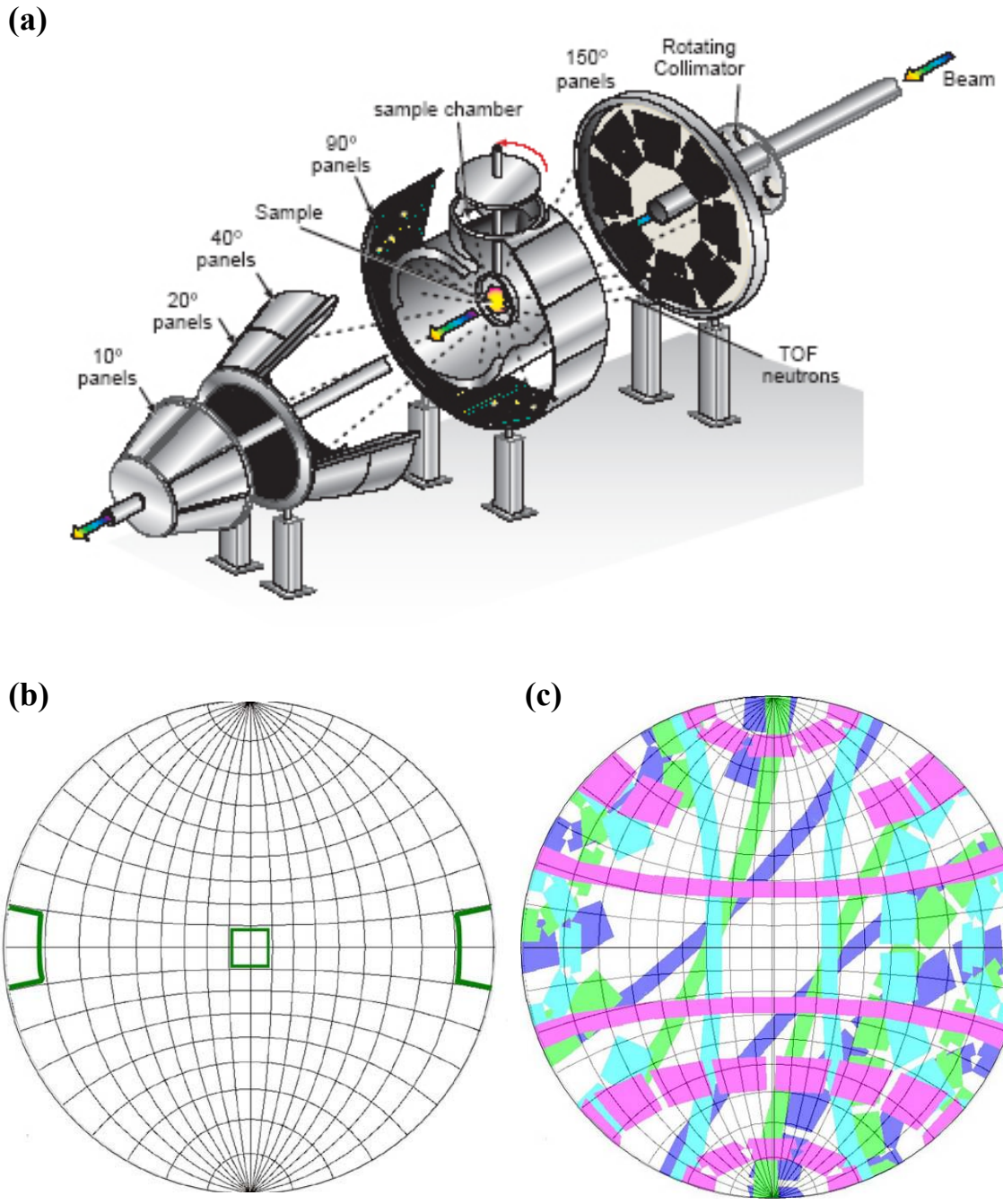

Figure 4.17 (a) HIPPO schematic showing the placement of detectors. (b) SMARTS detector coverage on a stereographic projection. (c) HIPPO detector coverage.

pseudoelasticity in Fe_3Al. CRATES is a uni-axial stress-rig which allows *in situ* tensile and compression experiments.

4.3.1 *In situ* tensile experiment in HIPPO

Due to the limited detector coverage of SMARTS (Figure 4.17) most of the low index peaks of single crystal Fe_3Al could not be detected. In order to have more detector coverage and thus to be able to gather information about the behavior of other peaks, *in situ* tensile experiments were conducted in the HIPPO diffractometer. Dog bone shaped tensile specimen was loaded in tension in the <418> direction. Similar to the SMARTS experiments, the specimen was at 45^o to the beam direction.

The results of the findings are summarized in Figure 4.18. Each ring of detectors in HIPPO is divided into ten detector panels. Three of the ten detector panels of the 40 degree bank which show some interesting activity of low index peaks have been plotted in the figure. Since the HIPPO diffractometer is only ~9m from the moderator the resolution of the time of flight and hence the d-space is not as good as the SMARTS diffractometer (~32m from the moderator). Therefore, it was necessary to plot the data one panel at a time and thus get rid of unwanted background from the other panels which did not contain any low index peaks.

Since more applied strain can be recovered during tensile loading (chapter 3) as compared to compression, the samples were strained to ~ 6.1 % before they were unloaded. As with the SMARTS experiments, these experiments also showed big

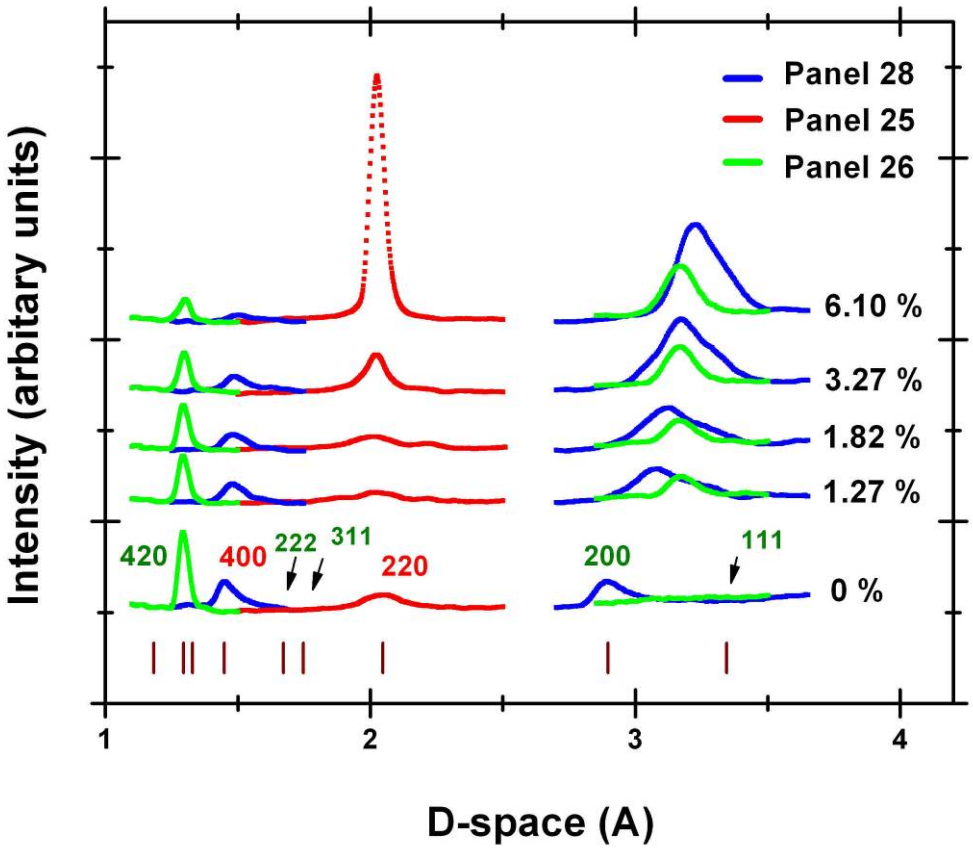

Figure 4.18 The evolution of diffraction pattern as a function of strain during tension experiment in HIPPO. Only the interesting detector panels have been included.

changes in the diffraction pattern. Upon unloading, the sample recovered most of the applied strain and the diffraction pattern was again close to the original diffraction pattern without load.

The specific peak behavior of some of the major peaks that were detected in these experiments was somewhat different from the SMARTs experiments. For example, the 400 peak intensity in this case decreased as compared to the 400 peak in the transverse bank of SMARTS which increased (Figure 4.9). The 200 peak seemed to move to a higher d-spacing and grow in intensity. However it was not clear, whether in fact was the original 200 peak. The resulting diffraction pattern may be a superposition of the 200 and a completely new peak.

Another broad new peak similar to it and at approximately the same position was observed in another detector panel (panel 26). This new peak appeared at a d-spacing where no $D0_3$ peak was expected. The 220 peak intensity increased by a huge amount. Again it was not clear from the data whether the resulting big peak was the original peak or the superposition of the 220 peak and a new peak. The change in the peak position of both 200 and 220 (if indeed they were the original peak) was orders of magnitude higher than that expected from elasticity. Also notable was the fact that the broad peak near the 200 reflection was similar in broadness and peak position to the broad peak that appeared near the 200 reflections in the SMARTS transverse bank (Figure 4.14).

4.4 Shape memory effect

The details of the shape memory effect shown by single crystal Fe_3Al have already been discussed in chapter 3. In this section results of low temperature experiment done in the SMARTS diffractometer are reported. The sample was taken through a full shape memory thermo-mechanical cycle and neutron diffraction patterns were taken at various points along this cycle.

The sample used in this case was a cylindrical sample with a diameter of 6 mm and a length of 14.4 mm. The sample was aligned for compression in the <418> direction. A low temperature furnace based on cryogenic cooling was used at the SMARTS instrument. The low temperatures were achieved by using special grips through which liquid nitrogen flows at a controlled rate. The temperature was monitored by low temperature thermocouples located at various locations along the grips. The temperature was controlled by controlling the flow rate of liquid nitrogen in the grips. Temperatures as low as 95 K can be achieved using this system.

In the first part of the experiment the sample was taken to low temperatures without any load. Diffraction patterns were taken at various points during the cooling process. Unlike conventional shape memory alloys like NiTi, Fe_3Al did not show any phase transformation upon cooling to ~95 K.

The sample was then compressed to ~3 % total strain at this low temperature. None of the applied strain was recovered upon unloading as seen in Figure 4.19. The diffraction pattern however, changed in a similar way as the room temperature experiments.

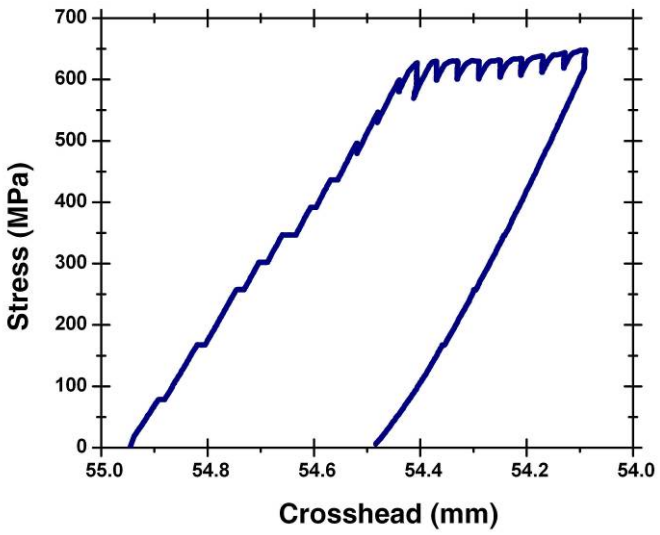

Figure 4.19 Compression stress-strain curve at ~95 K. No recovery occurs upon unloading.

Figure 4.20 (a) through (d) show the effect of loading on the diffraction pattern. Most notably, the 200 peak intensity decreases drastically. Other peaks also change in a similar way.

The sample is then heated up and brought up to room temperature. Throughout the heating process a very small load (~10 MPa) is applied to hold the sample in place. Also the machine is kept in load control mode so that the crosshead would move so as to keep the constant 10 MPa load on the sample. The crosshead movement was monitored as the sample was heated up (Figure 4.21). Since the temperature of the sample was ~95 K at the beginning of this part of the experiment there was a significant amount of thermal contraction of the samples as well as the grips etc.

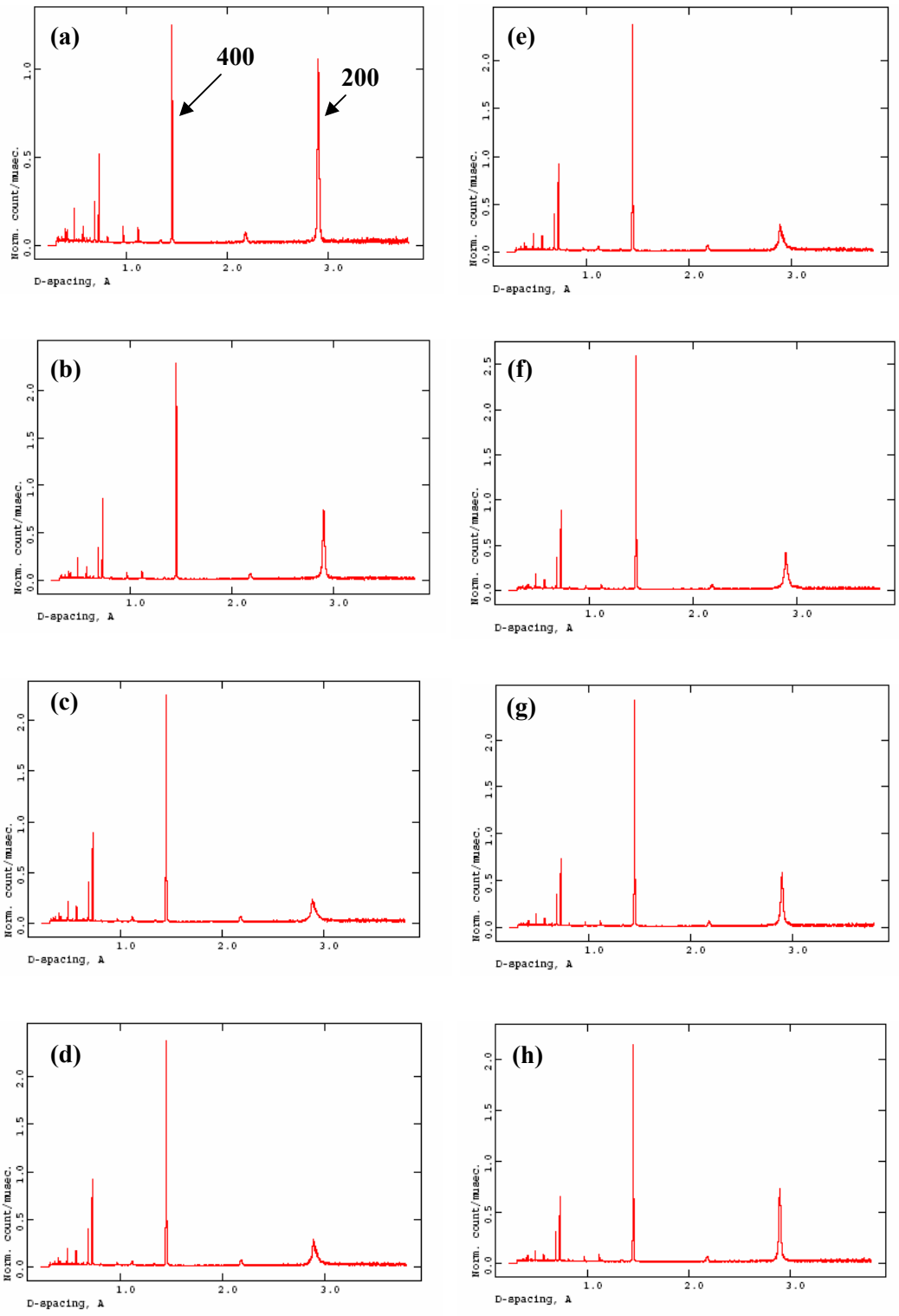

Figure 4.20 Diffraction Patterns (a)-(d) low temperature compression. (e)-(h) recovery upon heating (shape memory).

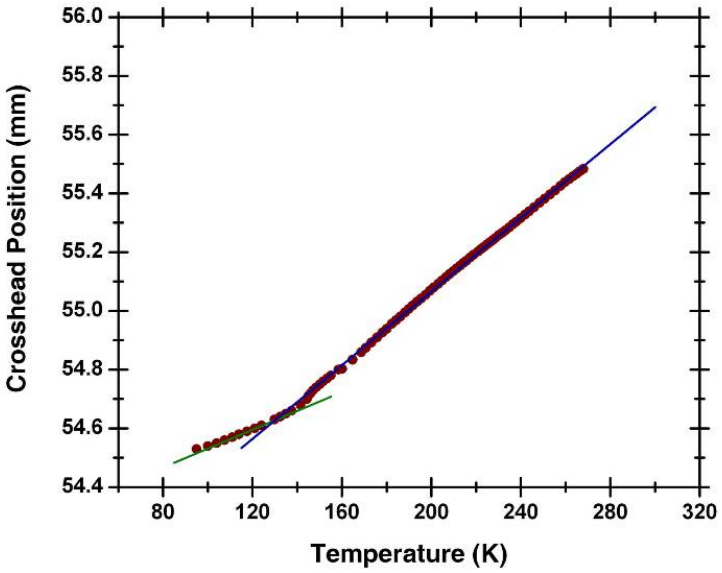

Figure 4.21 The change in slope of the crosshead movement (at constant load control) with temperature marks the commencement of shape memory type recovery.

As the sample was heated the sample and the grips expanded in a linear way. At approximately 140 K, there was a significant change in the slope of this line. After the sample was at room temperature the measured length showed that almost all the applied strain was recovered. The change in slope corresponded to the commencement of recovery of the shape memory material.

Throughout this cycle diffraction patterns were recorded. These are shown in Figures 4.20 (e) through (h). The peak intensity of the 200 peak was plotted as a function of the run number (Figure 4.22) which corresponds to the sequence of events described above. Note that the intensity does not return to the original value. This may be due to a time dependent component of the recovery as discussed in chapter 3.

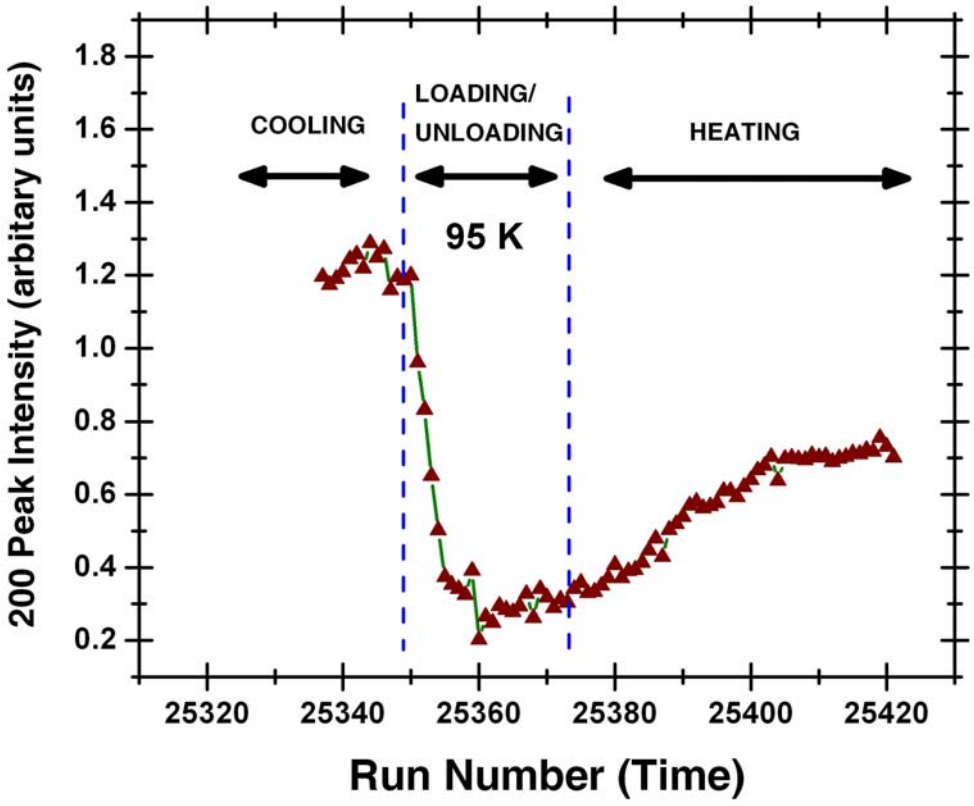

Figure 4.22 The 200 peak intensity during different parts of the shape memory cycle.

4.5 Mechanism

The changes in diffraction pattern upon loading points towards some change in the structure of material. There could be two possible reasons for these big changes in the diffraction pattern. One, changes have occurred in the crystal lattice. Two, the lattice has reoriented or a rotation has occurred in effect (e.g. twin). Since the SMARTS detectors are small in size it was thought that a rotation could be responsible for the peak intensity changes. Therefore, simulations of what happens when certain twins form were done in order to explain the observed changes. After the data were carefully analyzed it was concluded that they could not be explained by a rotation in the crystal lattice.

In chapter 1 three possible mechanisms were discussed. Twins can be eliminated because no rotation was observed. It is also highly unlikely that the APB mechanism is operative. Although the passage of partial dislocations would increase the disorder in the crystal, huge changes in peak intensities are not expected from such dislocation motion. Furthermore it is unable to explain the new peaks and satellite reflections.

The occurrence of new peaks (Figure 4.14, 4.15 and 4.18) and satellite reflections (Figure 4.16) suggests that a phase transformation is the most likely operative mechanism for pseudoelasticity in Fe_3Al. Unfortunately a full detailed diffraction pattern could not be obtained from either of the neutron diffractometers (HIPPO or SMARTS) and therefore the details of this transformation could not be determined using the current data.

Chapter # 5

Conclusions and Future Work

5.1 Conclusions

Fe_3Al single crystal shows pseudoelastic and shape memory behavior in the <418> loading direction. Strains up to 10% were recovered in tension, with a big stress-strain hysterisis. Less strain was recovered during compressive loading where the stress-strain curve also showed strain hardening. Parallel step lines appeared on the sample surface corresponding to the pseudo-elastic straining, which disappeared on removal of the strain. These were shown to be traces of the (211) planes. Wavy slip lines were seen on samples strained beyond the recoverable limit, which did not disappear after unloading. These slip lines trapped some of the parallel step lines. Pseudo-elastic recovery in Fe_3Al was found to be a function of time. At temperatures higher than or equal to 120^{o}C, pseudo-elasticity was lost. Shape memory effect was observed under tension and compression at very low temperatures (~ -178^{o}C). The unloading part of the tensile stress-strain curve showed that the variation of recovery stress with temperature followed the Clausius-Clapeyron law. Although the nature of pseudo-elasticity in single crystal Fe_3Al has many of the same characteristics as well known SMAs, Fe_3Al does not show all the physical effects of SMAs.

Neutron diffraction patterns as a function of a strain showed large reversible changes in peak intensities. The changes in the superlattice and the fundamental peak intensities of the same family varied in different ways. Certain broad new peaks and satellite reflections appeared upon loading. All these changes in the diffraction pattern were reversible and the diffraction pattern went back close to the original pattern upon unloading of the sample. It was concluded that the changes in diffraction pattern did not represent any rotation indicative of twin formation. The appearance of new peaks pointed towards a possible phase transformation.

5.2 Future work

The details of the transformation that is responsible for pseudoelasticity in Fe_3Al needs to be studied. Additional diffraction experiments have to be done in a diffractometer which is specifically built for single crystals with better spatial resolution.

References

[1] Suathoff G. Intermetallics. Weinheim: Wiley-VCH, 1995.

[2] Intermetallic compounds : Principles and practice. Chichester: John Wiley & Sons, 1995.

[3] Intermetallic compounds : Progress. Chichester: John Wiley & Sons, 2002.

[4] Sikka VK. High Temperature Aluminides and Intermetallics: Commercialization of Nickel Aluminides. In: Whang SH, Liu CT, Pope DP, Stiegler JO, editors. TMS Fall Meeting. Indianapolis, IN, 1989. p.505.

[5] Otsuka K, Wayman CM. Shape memory materials. New York: Cambridge University Press, 1998.

[6] Buschow KHJ. New Developments in Hard Magnetic-Materials. Reports on Progress in Physics 1991;54:1123.

[7] Hill HH, Matthias BT. Study of Superconductivity of Intermetallic Compounds U6mn U6fe U6co and U6ni and Alloys Formed between Them. Physical Review 1968;168:464.

[8] Stoloff NS, Davies RG. Mechanical Properties of Ordered Alloys. Progress in Materials Science 1966;13:3.

[9] Cullity BD. Elements of X-Ray Diffraction. Upper Saddle River, NJ: Prentice Hall, 2001.

[10] Ziegler N. Resistance of Iron-Aluminum Alloys to Oxidation at High Temperatures. AIME Transactions 1932;100:267.

[11] Sykes C, Bampfylde J. The Physical Properties of Iron-Aluminum Alloys. Journal of Iron and Steel Institute 1934;130:389.

[12] Kear BH. Dislocation Configurations + Work Hardening in Cu3au Crystals. Acta Metallurgica 1964;12:555.

[13] Blackburn MJ. Boeing Scientific Research Labs, 1963.

[14] Liu CT, George EP, Maziasz PJ, Schneibel JH. Recent advances in B2 iron aluminide alloys: deformation, fracture and alloy design. Materials Science and Engineering a-Structural Materials Properties Microstructure and Processing 1998;258:84.

[15] McKamey CG, DeVan JH, Tortorelli PF, Sikka VK. A review of recent developments in Fe_3Al-based alloys. J. Mater. Res. 1991;6:1779.

[16] Tomaszewicz P, Wallwork GR. Iron-Aluminum Alloys: A Review of Their Oxidation Behaviour. Review of High Temperture Materials 1978;4:76.

[17] Hardwick D, Wallwork G. Iron-Aluminum Base Alloys: A Review of Their Feasibility as High Temperature Materials. Review of High Temperture Materials 1978;4:47.

[18] Nachman JF, Buehler WJ. Application, Properties and Fabrication of Thermenol Type Alloys. Silver Spring, MD: U.S. Naval Ordnance Laboratory, 1956.

[19] Sikka VK, McKamey CG, Howell CR, Baldwin RH. Fabrication and Mechanical Properties of Fe_3Al-based Aluminides. Oak Ridge, TN: Oak Ridge National Laboratory, 1990.

[20] McKamey CG. Proceedings of the Four Annual Conference on Fossil Energy Materials Oak Ridge National Laboratory, Oak Ridge, TN, 1990. p.197.

[21] Ikeda O, Ohnuma I, Kainuma R, Ishida K. Phase equilibria and stability of ordered BCC phases in the Fe-rich portion of the Fe-Al system. Intermetallics 2001;9:755.

[22] Nachman JF, Buehler WJ. The Fabrication and properties of 16-Alfenol - A New Strategic Aluminum-Iron Alloy Silver Spring, MD: U.S. Naval Ordnance Laboratory, 1953.

[23] Nachman JF, Buehler WJ. Thermenol, A Non-Strategic Aluminum-Iron Base Alloy for High Temperature Service. Silver Spring, MD: U.S. Naval Ordnance Laboratory, 1954.

[24] Nachman JF, Buehler WJ. Application and Properties of Iron (10-17)% Aluminum Alloy. Silver Spring, MD: U.S. Naval Ordnance Laboratory, 1955.

[25] Iron-Aluminum Alloy Systems. Wright Patterson AFB,OH: Wright Air Developement Center, 1957-59.

[26] Justusson W, Zakay VF, Morgan ER. The Mechanical Properties of Iron-Aluminum Alloys. Trans. ASM 1957;49:905.

[27] Stoloff NS, Davies RG. Plastic deformation of ordered FeCo + Fe_3Al Alloys Acta Metallurgica 1964:473.

[28] Leamy HJ. The Plastic Deformation Behaviour of Long Range Ordered Iron-Aluminum Alloys. vol. PhD: Iowa State University, 1967.

[29] Leamy HJ, Gibson ED, Kayser FX. The Elastic Stiffness Coefficients of Iron-Aluminum Alloys--I-Experimental Results and Thermodynamic Analysis. Acta Metallurgica 1967;15:1827.

[30] Leamy HJ. The Elastic Stiffness Coefficients of Iron-Aluminum alloys--II-The Effect of Long Range Order. Acta Metallurgica 1967;15:1839.

[31] Leamy HJ, Kayser FX. The Compressive Deformation Behavior of Long Range Ordered Polycrystalline Iron-Aluminum Alloys. Phys. Status Solidi 1969;34:765.

[32] Leamy HJ, Kayser FX, Marcinkowski MJ. The Plastic Deformation Behaviour of Long-range Ordered Iron-Aluminum Alloys, I. Single Crystal Deformation Experiments. Philosophical Magazine 1969;20:763.

[33] Leamy HJ, Kayser FX, Marcinkowski MJ. II Transmission Electron Microscopical Observations. Philosophical Magazine 1969;20:779.

[34] Marcinkowski MJ, Taylor ME, Kayser FX. Relationship between Atomic Ordering and Fracture in Fe-Al Alloys. Journal of Materials Science 1975;10:406.

[35] Bordeau RG. Development of Iron Aluminides. Wright-Patterson AFB, OH: Wright Aeronautical Laboratories, 1987.

[36] Culbertson G, Kortovich CS. Development of Iron-Aluminides. Wright-Patterson AFB, OH: Air Force Wright Aeronautical Laboratories, 1986.

[37] McKamey CG, Liu CT, Cathcart JV, David SA, Lee EH. Evaluation of Mechanical and Metallurgical properties of Fe_3Al-Based Aluminides Oak Ridge, TN: Oak Ridge National Laboratory 1986.

[38] Inouye H, Liu CT, Horton JA. Physical Metallurgy and Mechanical Properties of Iron Aluminides. Department of Navy, Arlington, VA: Oak Ridge National Laboratory for the Office of Naval Research 1982-1984.

[39] McKamey CG, Liu CT, David SA, Horton JA, Pierce DH, Campbell JJ. Developement of Iron Aluminides for Coal Conversion Systems. Oak Ridge, TN: Oak Ridge National Laboratory 1988.

[40] McKamey CG, Sikka VK, Zacharia T, David SA, Alexander DJ. Fossil Energy Advanced Research and Technology Development Materials Program Semiannual Progress Report. Oak Ridge , TN: U. S. Department of energy, 1990. p.235.

[41] Judkins RR, Braski DN. Proceedings of the Fourth Annual Conference on Fossil Energy Materials. Oak Ridge, TN U. S. Department of Energy, 1990.

[42] Davies RG. Kinetics of Ordering and Domain Hardening in Fe_3Al. TMS-AIME 1964;230:903.

[43] Lawley A, Coll JA, Cahn RW. Influence of Crystallographic Order on Creep of Iron-Aluminum Solid Solutions. TMS-AIME 1960;218:166.

[44] Marcinkowski MJ, Brown N. Theory and Direct Observation of Dislocations in the Fe_3Al Superlattices. Acta Metallurgica 1961;9.

[45] Crawford RC, Ray ILF, Cockayne DJH. The Weak-beam Technique Applied to Superlattice Dislocations in Iron-Aluminum Alloys, II. Fourfold Dissociation in D03-type Order. Philosophical Magazine 1973;27:1.

[46] Schroer W, Hartig C, Mecking H. Plasticity of $D0_3$ ordered Fe-Al and Fe-Al-Si single crystals. Zeitschrift fur Metallkunde 1993;84.

[47] Morris DG, Peguiron D, Nazmy M. Yield Stress and Stress Anomaly in an Fe3Al Alloy. Philosophical Magazine a-Physics of Condensed Matter Structure Defects and Mechanical Properties 1995;71:441.

[48] Brinck A, Neuhauser H. On the temperature dependence of the yield stress in Fe3Al single crystals in the range of 300 to 500 K. Intermetallics 2000;8:1019.

[49] Morris DG, Zhao P, Munoz-Morris MA. An examination of the influence of strain rate on the stress anomaly in Fe3Al. Materials Science and Engineering a-Structural Materials Properties Microstructure and Processing 2001;297:256.

[50] Morris DG, Munoz-Morris MA. The stress anomaly in FeAl-Fe3Al alloys. Intermetallics 2005;13:1269.

[51] Guedou JY, Paliard M, Rieu J. Pseudo-Elasticity in Ordered Fe-Al Alloys. Scripta Metallurgica 1976;10:631.

[52] Guedou JY, Rieu J. Twinning and Pseudo-Elasticity in Single-Crystal Fe-Al Alloys. Scripta Metallurgica 1978;12:927.

[53] Guedou JY, Rieu J. Effect of Crystal Orientation on Slip Geometry and Pseudo-Elastic Behavior in Fe3Al Alloys. Comptes Rendus Hebdomadaires Des Seances De L Academie Des Sciences Serie B 1978;286:327.

[54] Kubin LP, Fourdeux A, Guedou JY, Rieu J. Pseudoelasticity and Slip Reversibility in Do3-Ordered Fe-Al Single-Crystals by Insitu Experiments. Philosophical Magazine a-Physics of Condensed Matter Structure Defects and Mechanical Properties 1982;46:357.

[55] Dieter GE. Mechanical metallurgy. New York: McGraw-Hill, 1986.

[56] Callister WD. Materials science and engineering : an introduction. New York, NY: John Wiley & Sons, 2003.

[57] Ctsuka K, Wayman CM. Shape memory materials. New York: Cambridge University Press, 1998.

[58] Otsuka K, Sawamura T, Shimizu K, Wayman CM. Characteristics of Martensitic Transformation in Tini and Memory Effect. Metallurgical Transactions 1971;2:2583.

[59] Miyazaki S, Otsuka K. Deformation and Transition Behavior Associated with the R-Phase in Ti-Ni Alloys. Metallurgical Transactions a-Physical Metallurgy and Materials Science 1986;17:53.

[60] Otsuka K, Wayman CM, Nakai K, Sakamoto H, Shimizu K. Superelasticity Effects and Stress-Induced Martensitic Transformations in Cu-Al-Ni Alloys. Acta Metallurgica 1976;24:207.

[61] Jourdan C, Gastaldi J, Roques V, Grange G, Belkahla S, Guenin G. In-Situ Study of the Self-Accommodating Process During the Martensitic-Transformation of a Cu-Zn-Al Single-Crystal by Synchrotron X-Ray Topography .1. Crystallographic Study. Acta Metallurgica Et Materialia 1995;43:4213.

[62] Dunand DC, Mari D, Bourke MAM, Roberts JA. NiTi and NiTi-TiC composites .4. Neutron diffraction study of twinning and shape-memory recovery. Metallurgical and Materials Transactions a-Physical Metallurgy and Materials Science 1996;27:2820.

[63] Chernenko VA, Pons J, Segui C, Cesari E. Premartensitic phenomena and other phase transformations in Ni-Mn-Ga alloys studied by dynamical mechanical analysis and electron diffraction. Acta Materialia 2002;50:53.

[64] Khalil-Allafi J, Dlouhy A, Eggeler G. Ni4Ti3-precipitation during aging of NiTi shape memory alloys and its influence on martensitic phase transformations. Acta Materialia 2002;50:4255.

[65] Uchil J, Mohanchandra KP, Kumara KG, Mahesh KK. Study of critical dependence of stable phases in Nitinol on heat treatment using electrical resistivity probe. Materials Science and Engineering a-Structural Materials Properties Microstructure and Processing 1998;251:58.

[66] Okamoto H, Beck PA. Phase Relationships in Iron-Rich Fe-Al Alloys. Metallurgical Transactions 1971;2:569.

[67] Swann PR, Duff WR, Fisher RM. Electron Metallography of Ordering Reactions in Fe-Al Alloys. Metallurgical Transactions 1972;3:409.

[68] Oki K, Hasaka M, Eguchi T. Process of Order-Disorder Transformation in Iron-Aluminum Alloys. Japanese Journal of Applied Physics 1973;12:1522.

[69] Yasuda HY, Nakano K, Nakajima T, Ueda M, Umakoshi Y. Effect of ordering process on giant pseudoelasticity in Fe3Al single crystals. Acta Materialia 2003;51:5101.

[70] Langmaack E, Nembach E. Pseudoelasticity in Fe3Al single crystals. Philosophical Magazine a-Physics of Condensed Matter Structure Defects and Mechanical Properties 1999;79:2359.

[71] Nosova GI, Polyakova NA, Novikova YY. Nature of Pseudoelasticity Effect in Ordered Fe3Al Alloys. Fizika Metallov I Metallovedenie 1986;61:592.

[72] Brinck A, Engelke C, Neuhauser H. On pseudoelasticity in single crystals of the intermetallic compound Fe3Al. Scripta Materialia 1997;37:569.

[73] Yasuda HY, Nakano K, Ueda M, Umakoshi Y. Orientation dependence of pseudoelasticity in Fe3Al single crystals. Thermec'2003, Pts 1-5 2003;426-4:1801.

[74] Yasuda HY, Nakajima T, Nakano K, Yamaoka K, Ueda M, Umakoshi Y. Effect of Al concentration on pseudoelasticity in Fe3Al single crystals. Acta Materialia 2005;53:5343.

[75] Park KT, Goo E. Deformation Twinning in Do3-Ordered Fe3a1 Alloys. Acta Metallurgica Et Materialia 1991;39:3027.

[76] Bain EC. The nature of martensite. Transactions of the American Institute of Mining and Metallurgical Engineers 1924;70:25.

[77] Reed-Hill RE, Abbaschian R. Physical metallurgy principles. Boston: PWS-Kent Pub., 1992.

[78] Hirth JP, Lothe J. Theory of dislocations. New York: Wiley, 1982.

[79] Green ML, Cohen M. Pseudotwinning and Pseudoelasticity in Beta Fe-Be Alloys. Acta Metallurgica 1979;27:1523.

[80] Bacon GEGE. X-ray and neutron diffraction New York: Oxford, New York, Pergamon Press 1966.

[81] Warren BEBE. X-ray diffraction. Reading, Mass.: Addison-Wesley Pub. Co., 1969.

[82] Compton AH. The total reflexion of X-rays. Philosophical Magazine 1923;45:1121.

[83] Beeching R. Electron diffraction London: Methuen 1946.

[84] von Halban H, Preiswerk P. Experiemtal evidence of neutron diffraction. Comptes Rendus Hebdomadaires Des Seances De L Academie Des Sciences 1936;203:73.

[85] Saleh TA. Nondestructive evaluation of loading and fatigue effects in HAYNES 230 alloy 2006.

Vita

Saurabh Kabra was born in the ancient city of Varanasi (Benaras), India on April the 9th 1979. He grew up near the Ghats of the Ganges listening to the Shahnai of Pandit Bismillah Khan. By the time he graduated from St. John's High School his uncle had instilled a love for science and engineering in him. He graduated from the Indian Institute of Technology (IIT) Kanpur, India with a bachelor's degree in Mechanical Engineering in the May of 2002. He came to the United States to start his PhD degree and pursue his American dream. He worked on his PhD with a Materials Science major from August 02 till September 06 at the University of Tennessee, Knoxville, Oak Ridge National Laboratory, Oak Ridge and Los Alamos National Laboratory, Los Alamos. He worked as a research assistant during this period. He is still as fascinated with science as the day that he learnt that all matter is made of atoms and wishes to continue this learning process in the future.